AGU ADVANCING EARTH AND SPACE SCIENCES

Earth and Space Science

RESEARCH ARTICLE
10.1029/2023EA003121

# Evaluation of Different Bias Correction Methods for Dynamical Downscaled Future Projections of the California Current Upwelling System

**Mercedes Pozo Buil[1,2], Jerome Fiechter[3], Michael G. Jacox[1,2,4], Steven J. Bograd[1,2], and Michael A. Alexander[4]**

[1]Institute of Marine Sciences, University of California Santa Cruz, Santa Cruz, CA, USA, [2]NOAA Southwest Fisheries Science Center, Monterey, CA, USA, [3]Ocean Sciences, University of California Santa Cruz, Santa Cruz, CA, USA, [4]NOAA Physical Sciences Laboratory, Boulder, CO, USA

**Key Points:**

- Bias correcting forcing prior to downscaling is key to reducing historical biases and resolving critical ecosystem-relevant coastal processes
- Different bias correction methods produced similar mean and seasonal changes of ecosystem variables in downscaled projections
- Using forcing without bias correction amplified the historical bias of some variables and produced a misrepresentation of the California Undercurrent

**Supporting Information:**

Supporting Information may be found in the online version of this article.

**Correspondence to:**

M. Pozo Buil,
mercedes.pozo@ucsc.edu

**Citation:**

Pozo Buil, M., Fiechter, J., Jacox, M. G., Bograd, S. J., & Alexander, M. A. (2023). Evaluation of different bias correction methods for dynamical downscaled future projections of the California current upwelling system. *Earth and Space Science*, *10*, e2023EA003121. https://doi.org/10.1029/2023EA003121

Received 20 JUN 2023
Accepted 27 OCT 2023

**Author Contributions:**

**Conceptualization:** Mercedes Pozo Buil, Jerome Fiechter, Michael G. Jacox, Steven J. Bograd, Michael A. Alexander
**Data curation:** Mercedes Pozo Buil
**Formal analysis:** Mercedes Pozo Buil
**Investigation:** Mercedes Pozo Buil
**Methodology:** Mercedes Pozo Buil, Jerome Fiechter
**Project Administration:** Mercedes Pozo Buil
**Resources:** Mercedes Pozo Buil



**Abstract** Biases in global Earth System Models (ESMs) are an important source of errors when used to obtain boundary conditions for regional models. Here we examine historical and future conditions in the California Current System (CCS) using three different methods to force the regional model: (a) interpolation of ESM output to the regional grid with no bias correction; (b) a "seasonally-varying" delta method that obtains a season-dependent mean climate change signal from the ESM for a 30-year future period; and (c) a "time-varying" delta method that includes the interannual variability of the ESM over the 1980–2100 period. To compare these methods, we use a high-resolution (0.1°) physical-biogeochemical regional model to dynamically downscale an ESM projection under the RCP8.5 emission scenario. Using different downscaling methods, the sign of future changes agrees for most of the physical and ecosystem variables, but the spatial patterns and magnitudes of these changes differ, with the seasonal- and time-varying delta simulations showing more similar changes. Not correcting the ESM forcing leads to amplification of biases in some ecosystem variables as well as misrepresentation of the California Undercurrent and CCS source waters. In the non-bias corrected and time-varying delta simulations, most of the ecosystem variables inherit trends and decadal variability from the ESM, while in the seasonally-varying delta simulation the future variability reflects the observed historical variability (1980–2010). Our results demonstrate that bias correcting the forcing prior to downscaling improves historical simulations, and that the bias correction method may impact the spatial and temporal variability of the future projections.

**Plain Language Summary** Global Earth System Models (ESMs) are important tools to understand Earth's processes and project how they will change over time in response to anthropogenic activity and changing climate conditions. However, ESMs have limited capacity to resolve coastal processes at sufficiently high resolution (e.g., <50 km) and often show regional biases when they are compared to observed data. To address the resolution issue, ESMs can be used as input to force high-resolution models, and their biases with respect to observed data can be reduced by applying bias-correction methods. This process, called dynamical downscaling, is widely used; but, the implications of different methodological choices during downscaling have not been adequately explored. In this article, we compare three different pre-processing methods (two with bias correction and one without) prior to dynamical downscaling to simulate present and future conditions in the California Current System. We evaluate the performance of each method by comparing with observed data and assessing how they reproduce future changes and variability. We find that bias correcting the ESM data before forcing the ocean model is key to reducing ESM biases and resolving coastal processes. Results here will help to guide methodological choices when projecting climate change using high-resolution ocean models to resolve coastal processes.

## 1. Introduction

The California Current System (CCS) is a highly productive eastern boundary upwelling system (EBUS) that supports a variety of fisheries and marine services along the U.S. Pacific coast (e.g., Checkley & Barth, 2009; Pauly & Christensen, 1995). Assessing projected climate change and the impacts at regional and local scales is key to long-term planning and resource management in this highly productive ecosystem (Smith et al., 2023). Global climate models (GCM) and Earth System Models (ESMs) are primary tools for understanding the climate

**Software:** Mercedes Pozo Buil, Jerome Fiechter
**Validation:** Mercedes Pozo Buil
**Visualization:** Mercedes Pozo Buil
**Writing – original draft:** Mercedes Pozo Buil, Jerome Fiechter, Michael G. Jacox, Steven J. Bograd, Michael A. Alexander
**Writing – review & editing:** Mercedes Pozo Buil, Jerome Fiechter, Michael G. Jacox, Steven J. Bograd, Michael A. Alexander

system including ocean biogeochemistry and projecting future climate; however, their utility at regional and local scales is limited by their coarse resolution (~100–200 km), which does not allow them to represent key details of coastal and upwelling dynamics (e.g., Capet et al., 2004; Franco et al., 2018; Jacox et al., 2015; Mote & Mantua, 2002; Renault et al., 2016).

One method commonly used to fill this gap is dynamical downscaling, which produces high-resolution projections by using the information from coarser resolution models as initial and boundary conditions for regional models. Regional climate models (RCM) coupled one-way to GCMs/ESMs are commonly used for dynamical downscaling in atmospheric, hydrologic, and land focused studies (e.g., Giorgi et al., 2009; Giorgi et al., 2014; Tapiador et al., 2020), while for ocean and marine ecosystem applications, there is a recent increase of using uncoupled regional ocean models forced with ESMs. For examples of downscaled ESMs for ecosystem and coastal U.S. applications, the reader is referred to Table 1 in Drenkard et al. (2021). Through higher resolutions and improved regional parameterizations of finer-scale physical and biogeochemical processes, dynamical downscaling can recover important processes and interactions that are unrepresented by ESMs (e.g., Drenkard et al., 2021; Echevin et al., 2020; Kerkhoff et al., 2014; Machu et al., 2015). However, ESM biases can propagate through the boundaries of the regional domain (e.g., Machu et al., 2015), degrading the downscaled simulations and also acting as a source of uncertainty. Thus, bias correcting methods have the potential to significantly improve dynamical downscaling simulations (Bruyère et al., 2014; Machu et al., 2015; Xu & Yang, 2012).

A common method to correct biases in ESMs and improve downscaled ocean projections is the "delta method", in which the mean differences (deltas) between the historical and future periods are first derived from ESMs, and then added to the observed historical conditions prior to downscaling. Dynamical downscaled approaches using a RCM coupled to a GCM and uncoupled regional ocean models have been used previously to produce high-resolution climate projections for the CCS for short (~10–30 years) future periods (Arellano & Rivas, 2019; Auad et al., 2006; Dussin et al., 2019; Howard et al., 2020; Li et al., 2014; Xiu et al., 2018). Some of these previous high-resolution projections created the forcing by directly interpolating the ESM output onto the regional model grid, not considering the inherent present-climate bias in ESMs (Arellano & Rivas, 2019; Dussin et al., 2019; Xiu et al., 2018). Some of these studies downscaled one single ESM (e.g., Arellano & Rivas, 2019; Xiu et al., 2018) or applied idealized perturbations (Dussin et al., 2019) in some forcing variables, not accounting for the full range of future uncertainty. To correct for the present-climate bias in the ESMs, Howard et al. (2020) applied a delta method to some atmospheric and oceanic forcing variables and downscaled an ensemble of five ESMs for the CCS. In the Northwest Atlantic Ocean, Alexander et al. (2019) extended the delta method approach by retaining the seasonal cycle of the long-term deltas ("seasonally-varying deltas") and adding them to the atmospheric and oceanic forcing of their control simulation. Projections made applying these delta methods are usually short-term (~10–30 years depending on the time-span of their historical forcing period), represent future climate conditions over a discrete period (i.e., time-slice), and do not simulate the transient evolution of the climate system (~2020–2100). To bias correct the present-climate bias of ESMs while also incorporating changes in interannual variability and resolving the full transient period, a "time-varying" delta method was applied to an ensemble of ESMs that span the CMIP5 range of projected future changes for the CCS (Pozo Buil et al., 2021). In the "time-varying" delta method, the deltas are computed from the full period of interest relative to a historical period (more in methods sections). A similar method was applied in other EBUS (e.g., Humboldt Upwelling System, Echevin et al., 2020).

Despite the widespread use of dynamical downscaling for ocean projections, there is still no consensus on whether to use bias correction and, if used, which method is best (Drenkard et al., 2021). Improved understanding of the sensitivity of projected changes to this choice is needed. Here we compare three bias correction methods applied before dynamical downscaling, focusing on the response of variables that are important for ecosystems in the CCS. To describe sensitivities of the future projections to the bias correction method, we use only one ESM, the GFDL-ESM2M (Dunne et al., 2012). Although selecting a single ESM model among the entire CMIP5 archive (Taylor et al., 2012) limits the representation of the envelope of projected regional climate changes and uncertainties (e.g., Cheung et al., 2016; Frölicher et al., 2016), our focus here is not on uncertainties in the ESM forcing but on the differences due to the bias correction method. For the CCS, dynamical downscaled future climate-change scenarios using a single ESM are described in Arellano and Rivas (2019), and Snyder et al. (2003), and uncertainties of future changes using ensembles of downscaled projections are described in Howard et al. (2020) and Pozo Buil et al. (2021). The objective of this paper is to assess the impact of bias correcting the forcing prior to downscaling for regional ocean projections in the CCS, specifically by comparing two bias correction techniques

(i.e., seasonally- and time-varying deltas) with the uncorrected interpolation of the ESM forcing. We also assess the representation of a key circulation feature of the CCS, the California Undercurrent (CU), which is a narrow northward flowing current (~100–150 km wide), usually found over the continental slope between 150 and 500 m depth, extending from Baja California to Vancouver Island (e.g., Gómez-Valdivia et al., 2017; Huyer et al., 1998; Thomson & Krassovski, 2010).

This paper is organized as follows: Section 2 describes the regional ocean model, dynamical downscaling methods, and the datasets used; Section 3 comprises the results, shown for the three dynamical downscaling methods; and Section 4 presents a summary and discussion.

## 2. Models and Methods

### 2.1. Regional Coupled Physical-Biogeochemical Ocean Model

To compare the different bias correction methods, we use an implementation of the Regional Ocean Modeling System (ROMS) coupled with a biogeochemical model. ROMS is a free-surface, hydrostatic, primitive equation ocean model that uses stretched, terrain-following coordinates in the vertical and orthogonal curvilinear coordinates in the horizontal. Its advanced numerical algorithms and grid-structure make ROMS well suited for modeling coastal regions characterized by complex bathymetry and coastlines (Haidvogel et al., 2008; Shchepetkin & McWilliams, 2005). Here we use a ROMS configuration developed and implemented by the University of California Santa Cruz (http://oceanmodeling.ucsc.edu/) for the CCS (Veneziani et al., 2009). The model domain extends from 30°N to 48°N and 115–134°W (midway down Baja California to south of Vancouver Island, and ~1,000 km offshore) at 0.1° (~10 km) horizontal resolution with 42 terrain-following vertical layers.

The biogeochemical model (NEMUCSC) is a nutrient-phytoplankton-zooplankton (NPZ) model based on the North Pacific Ecosystem Model for Understanding Regional Oceanography (NEMURO, Kishi et al., 2007) and specifically developed and parameterized for the CCS region (Fiechter et al., 2014, 2018). NEMUCSC includes three limiting macro-nutrients (nitrate, ammonium and silicic acid), two phytoplankton groups (nanophytoplankton and diatoms), three zooplankton groups (micro-, meso-, and predatory zooplankton), three detritus pools (dissolved and particulate organic nitrogen and particulate silica), and oxygen and carbon cycling (Cheresh & Fiechter, 2020; Fiechter et al., 2018). The regional coupled biophysical ocean model will be hereafter referred to as "ROMS-NEMUCSC".

### 2.2. ROMS-NEMUCSC Control Simulation

We first use ROMS-NEMUCSC to perform a control simulation (hereafter CTRL) of the recent past from 1980 to 2010. Initial and ocean lateral boundary conditions are derived from the Simple Ocean Data Assimilation version 2.1.6 (SODA; Carton & Giese, 2008). The atmospheric surface forcing is derived from fifth generation global atmospheric reanalysis from the European Center for Medium-Range Weather Forecasts (ERA-5; Hersbach et al., 2020) at 1-hr and ~30 km resolution except for the surface winds, which are derived from ERA-5 for 1980–1987 and from the Cross-Calibrated Multi-Platform wind product (CCMP1; ~25 km; Atlas et al., 2011) for 1988–2010 at 6-hr resolution. Concatenating these two wind analyses to force ROMS, improved nearshore currents relative to using just the ERA-5 winds, as described by Neveu et al. (2016). Air-sea fluxes are computed in ROMS internally using bulk formulae (Fairall, Bradley, Rogers, et al., 1996; Fairall, Bradley, Godfrey, et al., 1996; Liu et al., 1979). Physical variables are stored daily and used to force the biogeochemical component (i.e., NEMUCSC) "offline". Initial and boundary conditions for nitrate, silicate, and dissolved oxygen are derived from the monthly World Ocean Atlas climatology (WOA; Conkright et al., 2002). The initial and boundary conditions for ammonium, phytoplankton, zooplankton, and detritus are prescribed to a constant 0.1 mmol N $m^{-3}$. Details about carbonate variables can be found in Cheresh and Fiechter (2020) but are not considered in our analysis. Validation of the CTRL simulation is described in Pozo Buil et al. (2021).

### 2.3. Earth System Model

We selected the Geophysical Fluid Dynamics Laboratory (GFDL) ESM2M model to provide the atmospheric and oceanic forcing for the downscaled experiments with ROMS-NEMUCSC. The objective of this paper is to evaluate bias correction methods prior to downscaling, not model or scenario differences, so for our experiments

**TABLE 1**
*Downscaling Experiments Conducted With ROMS-NEMUCSC*

| Experiment (simulation period) | Atmospheric forcing | Ocean boundary/initial conditions | BGC boundary/initial conditions | Bias correction method |
|---|---|---|---|---|
| Control run, CTRL (1980–2010) | Hourly ERA-5 (heat fluxes), 6 hr ERA5 and CCMP1 winds | Monthly SODAv.2.1.6 | Monthly climatology WOA | None |
| Interpolation, INT (1980–2100) | Monthly GFDL | Monthly GFDL | Annual GFDL | None |
| Seasonally-Varying Delta, SV (2070–2100) | CTRL forcing + monthly GFDL | Monthly SODAv.2.1.6 + GFDL | Monthly climatology WOA + annual GFDL | Seasonally-Varying Delta |
| Time-Varying Delta, TV (1980–2100) | CTRL forcing + monthly GFDL | Monthly SODAv.2.1.6 + GFDL | Monthly climatology WOA + annual GFDL | Time-Varying Delta |
| $TV_{ATM}$ (1980–2100) | CTRL forcing + monthly GFDL | Monthly GFDL | Annual GFDL | Time-Varying Delta applied to atmospheric forcing |
| $TV_{OCE}$ (1980–2100) | Monthly GFDL | Monthly SODAv.2.1.6 + GFDL | Annual WOA + GFDL | Time-Varying Delta applied to oceanic forcing |

we employ a single ESM configuration (GFDL-ESM2M under RCP8.5) that has been widely used in previous climate and downscaling studies in the CCS (e.g., Dussin et al., 2019; Howard et al., 2020; Pozo Buil et al., 2021; Rykaczewski & Dunne, 2010; Rykaczewski et al., 2015; Xiu et al., 2018).

The GFDL-ESM2M coupled model (Dunne et al., 2012, GFDL hereafter) has a resolution of 2.5° longitude × 2° latitude with 24 vertical levels in the atmosphere and 1° longitude × 0.3–1° latitude in the ocean with 50 vertical levels. The atmospheric component is the Atmospheric Model version 2 (AM2; Anderson, 2004), the physical ocean component is GFDL's Modular Ocean Model version 4.1 (MOM4p1; Griffies et al., 2009), and the ocean biogeochemical component is the Tracers of Ocean Phytoplankton with Allometric Zooplankton code version 2.0 (TOPAZ2; Dunne et al., 2012, 2013). In this study, we combine the GFDL-EMS2M historical simulation (years 1980–2005) and the RCP 8.5 scenario (years 2006–2100).

### 2.4. Downscaling Experiments

Using three bias correction approaches, we conducted a set of experiments with the ROMS-NEMUCSC driven by GFDL (see Table 1).

#### 2.4.1. Direct Interpolation

In the first experiment (hereinafter referred to as INT), we directly interpolated the coupled climate model output onto the horizontal and vertical CCS regional grid to create the atmospheric, oceanic, and biogeochemical ROMS-NEMUCSC forcing. Recent studies have applied this method to the coast of the CCS (Xiu et al., 2018) and Baja California (Arellano & Rivas, 2019). All forcing variables are interpolated to the ROMS-NEMUCSC grid by applying a linear interpolation method to the atmospheric variables and cubic interpolation method to the ocean boundary variables.

#### 2.4.2. Seasonally-Varying Delta Method

Prior to explaining the delta methods applied in this study, we clarify that here we refer to the traditional delta method as "fixed" (i.e., "time-invariant") delta, where the future climate anomalies are calculated by subtracting the coupled climate models historical annual mean (e.g., 1980–2010) from the long-term future annual mean (e.g., 2070–2100) and then adding it to realistic historical conditions (e.g., Auad et al., 2006). This method removes the mean bias for the present-day climate of the coupled climate models and is intended to represent the mean climate change, assuming no change in spatiotemporal variability at the domain boundaries. However the seasonality and interannual variability are identical to those in the current climate.

Following Alexander et al. (2019), we extend the "fixed" delta method by retaining the seasonal cycle of the long-term deltas and adding them to the atmospheric, oceanic, and biogeochemical forcing of our CTRL simulation. Each bias-corrected forcing variable $X'$ is then computed as follows:

$$X'_{2070-2100} = REAN_{1980-2010} + (ESM_{CLM,2070-2100} - ESM_{CLM,1980-2010}) \quad (1)$$

where $REAN_{1980\text{-}2010}$ represents the observed historical forcing obtained from atmosphere and ocean reanalyzes, and $ESM_{CLM}$ corresponds to the mean seasonal cycle of the GFDL forcing variables for the future period (i.e., 2070–2100) and the historical period (i.e., 1980–2010). The difference of the mean seasonal cycles between the two periods creates the seasonally-varying deltas as monthly averages. The seasonally-varying deltas are first bilinearly interpolated in space and with a cubic spline in time to the resolution of the reanalysis data we used to force the CTRL run, and added to them. All bias-corrected forcing variables are then interpolated to the ROMS-NEMUCSC grid by applying a linear interpolation method to the atmospheric variables and cubic interpolation method to the ocean boundary variables. In this experiment, both the mean climate and its seasonality may change, but the interannual variability is still fixed to the current climate. We refer to this second experiment as SV.

10.1029/2023EA003121



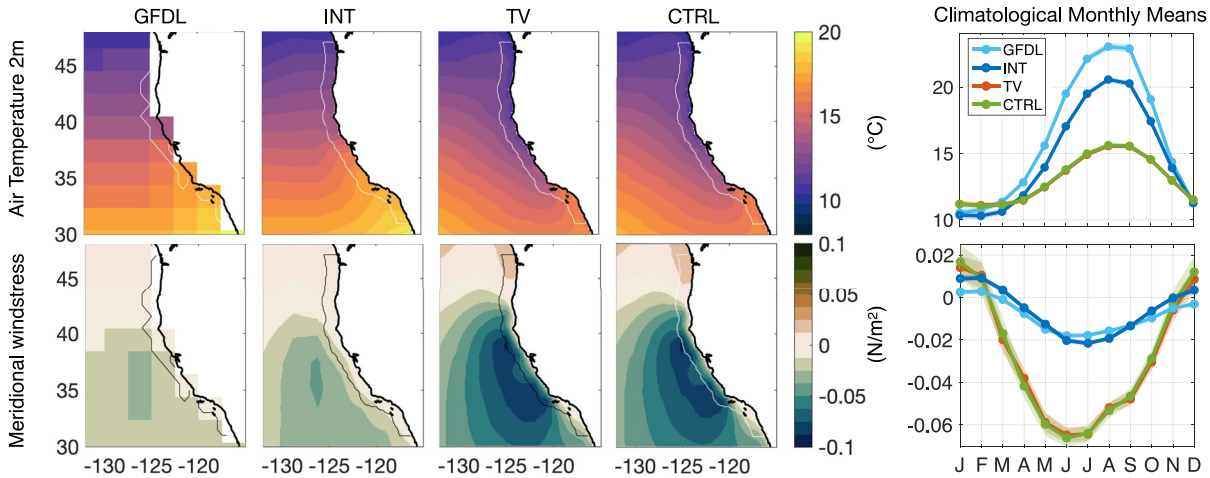


**Figure 1.** Annual mean of selected forcing variables for the historical period (1980–2010). (top) Air temperature at 2 m, and (bottom) meridional wind stress at 10 m for the (left) GFDL output, (second column) INT, (third column) TV, and (fourth column) CTRL run. The CTRL run represents the historical period of SV. The black/white lines on the maps represent a 100 km distance from the coast. (right) Historical monthly mean of the forcing variables averaged from the coast to 100 km offshore. Shading represents the monthly standard error of the forcing variables.

### 2.4.3. Time-Varying Delta Method

Following Pozo Buil et al. (2021), we first calculate the time-varying deltas by subtracting the coupled climate model historical monthly climatology ($ESM_{CLM}$; years 1980–2010) from the whole period of interest (1980–2100). We also compute the monthly climatology ($REAN_{CLM}$) and high-frequency variability ($REAN_{HF}$) from the reanalysis used to force the control run. The high frequency variability is computed as the residual after removing a running mean with a window length of 30 days. The time-varying deltas are then added to the monthly climatology ($REAN_{CLM}$) and daily variability ($REAN_{HF}$). Since $REAN_{HF}$ is only 30 years long, it is repeated (~4 times) to cover the whole period of interest. The time-varying deltas are bilinearly interpolated in space and using a cubic spline in time to match the reanalysis temporal resolution. All bias-corrected forcing variables are then interpolated to the ROMS-NEMUCSC grid by applying a linear interpolation method to the atmospheric variables and a cubic interpolation method to the ocean boundary variables. For each atmospheric forcing variable X, the bias-corrected variable by the time-varying delta method $X'$ is computed as follows:

$$X'_{1980-2100} = (REAN_{CLM,1980-2010} + REAN_{HF,1980-2010}) + (ESM_{1980-2100} - ESM_{CLM,1980-2010}) \quad (2)$$

The physical and biogeochemical ocean boundary conditions for the CTRL run have monthly and annual temporal resolution respectively, so those bias-corrected variables are computed excluding the high-frequency variability component ($REAN_{HF}$) in Equation 2. The daily variability is included only in the bias-corrected atmospheric forcing variables. The time-varying forcing inherits its climatological seasonal cycle and daily variability from the reanalysis products, while the interannual and long-term change comes from the ESM. Thus, the temporal and spatial resolution of the forcing is improved relative to the ESM, though the climate change signal of the forcing is at the ESM resolution. Similar methods to bias correct the forcing from coupled climate models have been used in dynamical downscaling studies of other upwelling systems (Cambon et al., 2013; Echevin et al., 2012, 2020; Oerder et al., 2015). We refer to this experiment as TV.

Examples of forcing variables for the different experiments are shown in Figures 1 and 2. During the historical period, large differences in the magnitude of forcing variables highlight the historical bias of the GFDL: higher air temperature along the coast during the summer months and weaker meridional wind stress in both the GFDL output and INT simulation (Figure 1). Here we use the term bias in the context of systematic errors in the model, as compared to a base "truth", the CTRL run. The future changes (deltas) of the three downscaled experiments resemble the same spatial pattern as the GFDL output, but can represent finer-scale features (Figure 2).

### 2.4.4. California Undercurrent Sensitivity Downscaling Experiments

To further examine how the bias correction method and downscaling choices influence the circulation, we present a more detailed case study of the California Undercurrent (CU)—a key dynamical feature off the North American

10.1029/2023EA003121

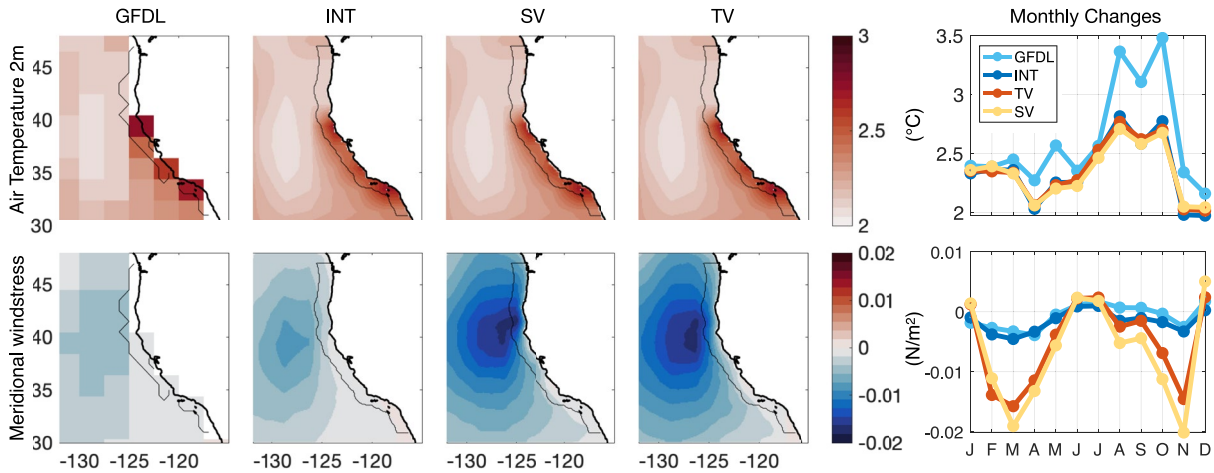


**Figure 2.** Future changes (2070–2100 relative to historical) of (top) air temperature at 2 m, and (bottom) meridional wind stress at 10 m for the (left) GFDL output, (second column) INT, (third column) SV, and (fourth column) TV. (right) The black line represents a 100 km distance from the coast. Future monthly changes averaged from the coast to 100 km offshore.

west coast i.e., often not well resolved in ESMs. In that regard, we explore the relative influences of atmospheric and ocean forcing on the regional simulation by conducting two additional sensitivity experiments: (a) bias correcting only the local atmospheric forcing and directly interpolating the oceanic open boundary conditions from the GFDL output ($TV_{ATM}$) and, (b) bias correcting only the remote oceanic open boundary conditions and directly interpolating the atmospheric forcing from the GFDL output ($TV_{OCE}$, Table 1). Here we refer to direct interpolation, as not applying any bias correction method to the forcing (i.e., same as described in 2.4.1).

### 2.5. Observational Datasets

To evaluate the downscaling simulations during the historical period, we use a set of high-resolution satellite and in situ-derived data sets. For sea surface temperature (SST), we use the Optimum Interpolation SST data set from the National Oceanic and Atmospheric Administration (NOAA OISST v2; Reynolds et al., 2007) at 0.25° from 1982 to 2010; for chlorophyll (CHL), we use data from the Sea-viewing Wide Field-of-view Sensor (SeaWiFS) obtained from the National Aeronautics and Space Administration (NASA) Ocean Color Website (NASA Goddard Space Flight Center, Ocean Ecology Laboratory, Ocean Biology Processing Group, 2014) at ∼0.1° resolution from 2000 to 2010 (original period is 1998–2010). To facilitate comparisons, observed surface variables are bilinearly interpolated onto the models grid. We also validate three subsurface variables: mixed layer depth (MLD) and nitrate and dissolved oxygen concentrations at 150 m depth, which is a level deeper than the seasonal historical mixed layer depth (MLD) which ranges from 30 to 100 m in the whole domain (Chhak & Di Lorenzo, 2007). MLD is defined as the shallowest depth at which a difference in temperature, measured from the surface, reaches a threshold of 0.8°C (Kara et al., 2000). We validated the MLD using output from the 30-year regional ocean reanalysis produced by 4D-VAR assimilation of multiple remotely sensed and in situ physical data for the CCS from 1982 to 2010 (Neveu et al., 2016). For the subsurface oxygen and nitrate concentrations, we use climatological data from the World Ocean Atlas derived from the World Ocean Database (Garcia et al., 2010a, 2010b), the CSIRO Atlas of Regional Seas (CARS) climatology (Dunn & Ridgway, 2002; Ridgway et al., 2002), the California Cooperative Oceanic Fisheries Investigations (CalCOFI) and the gridded Newport Hydrographic (NH) Line (Risien et al., 2022).

### 2.6. Analysis Methods

We focus here on time scales longer than 5 years, so time series are low-pass filtered using a 10-year running mean. For each simulation, we also show: (a) the projected changes computed as the difference between the means of the two reference periods (i.e., 2070–2100 vs. 1980–2010), (b) the standardized change computed as the future change divided by the standard deviation of anomalies in the historical period, and (c) the percentage changes computed with respect to the mean in the historical period (Table 2). The standardized change allows for

representation of the future change in the context of natural variability (e.g., a future mean change of 2°C would have a greater standardized change in a system lower natural variability).

To explore whether downscaled output is more accurate and less biased than the GFDL output, we use the Added Value following Dosio et al. (2015):

$$AV = \frac{(X_{MODEL1} - X_{obs})^2 - (X_{MODEL2} - X_{obs})^2}{Max\left((X_{MODEL1} - X_{obs})^2, (X_{MODEL2} - X_{obs})^2\right)} \quad (3)$$

where X represents the variable of interest. Values of AV range from −1 to 1. A positive AV means that the dynamically downscaled simulation improves over the original GFDL output. This measure of added value pertains only to change in skill with respect to the model's capacity to represent historical patterns, not the added value for projected changes.

## 3. Results

### 3.1. Bias Correction Method Historical Validation

We first evaluate the performance of the bias correction approaches by comparing the historical climatological and monthly mean of modeled variables against observations in key physical and biogeochemical variables. In the "seasonally-varying" method the historical period is the same as in the CTRL run. With respect to the observational SST, the GFDL output presents a general warm bias in the CCS, and a weak cool bias in the northern coastal region (first row in Figure 3). The warm bias intensifies during the summer months reaching ∼6°C in the southern coastal part of the CCS. The INT reproduces a similar pattern of SST bias to the GFDL output in the offshore regions, however in the coastal regions, the warm bias is amplified, reaching ∼7°C in summer (first row in Figure 3). The amplification of the SST bias in the INT simulation is possibly due to a decrease of the sensible heat flux from the ocean (i.e., less cooling) during the summer months compared to the GFDL forcing (first rows in Figure 1 and Figure S1 in Supporting Information S1). In contrast, TV is able to reproduce a similar bias with respect to the observed SST as the CTRL simulation, reducing the warm GFDL historical bias to ∼1°C (first row in Figure 3).

The four historical simulations reproduce similar spatial patterns of the bias of the mixed layer depth (MLD), featuring a positive bias (deeper MLD) south of 39°N and a negative bias (shallower MLD) north of ∼39°N. Along the coast, these biases have a larger magnitude in the GFDL output and the INT simulation compared to the TV simulation. During winter, both the GFDL output and INT simulation simulate a deeper (∼20 m) MLD compared to observations along the coast, while TV MLDs are close to but slightly shallower (<10 m) than observed (second row in Figure 3).

With respect to biogeochemical variables, GFDL output and INT both exhibit a positive bias of subsurface dissolved oxygen concentration (∼60 mmol $m^{-3}$) especially in the nearshore waters of the southern CCS (<40°N), while the bias is reduced in the offshore waters of INT. TV and CTRL both exhibit a negative dissolved oxygen bias over the southern ∼⅔ of the domain. The two downscaled simulations exhibit a similar seasonal cycle of dissolved oxygen as the CTRL near the coast. However, in INT the annual mean value is much higher than in the other ROMS simulations as well as observations, and is closer to the GFDL output (third row right column in Figure 3). Biases of subsurface nitrate follow the spatial distribution of those from the subsurface oxygen but with an opposite sign: GFDL and INT both exhibit a negative bias (∼-15 mmol $m^{-3}$) especially in the nearshore waters, while TV and CTRL both exhibit a positive bias, with monthly means more similar to the observations (Figure S5 in Supporting Information S1). Similar biases are found when comparing the simulations to the other datasets (Figures S2 and S3 in Supporting Information S1).

Following Goebel et al. (2010) we computed the chlorophyll concentration as the total phytoplankton biomass (i.e., the sum of small and large phytoplankton in ROMS-NEMUCSC) using fixed ratios for C:N (106:16) and C:Chl (50:1 and 100:1 for small and large phytoplankton, respectively). Along the coast, both GFDL and INT exhibit a strong negative bias and practically no seasonal variability in contrast to observations. These low surface chlorophyll values are possibly due to a combination of a reduced meridional wind stress (considered here as a proxy of upwelling favorable winds, Figure 1), and a lower subsurface nutrient concentration (Figure S5 in Supporting Information S1) compared to the CTRL run. Both TV and CTRL exhibit similar positive chlorophyll

10.1029/2023EA003121



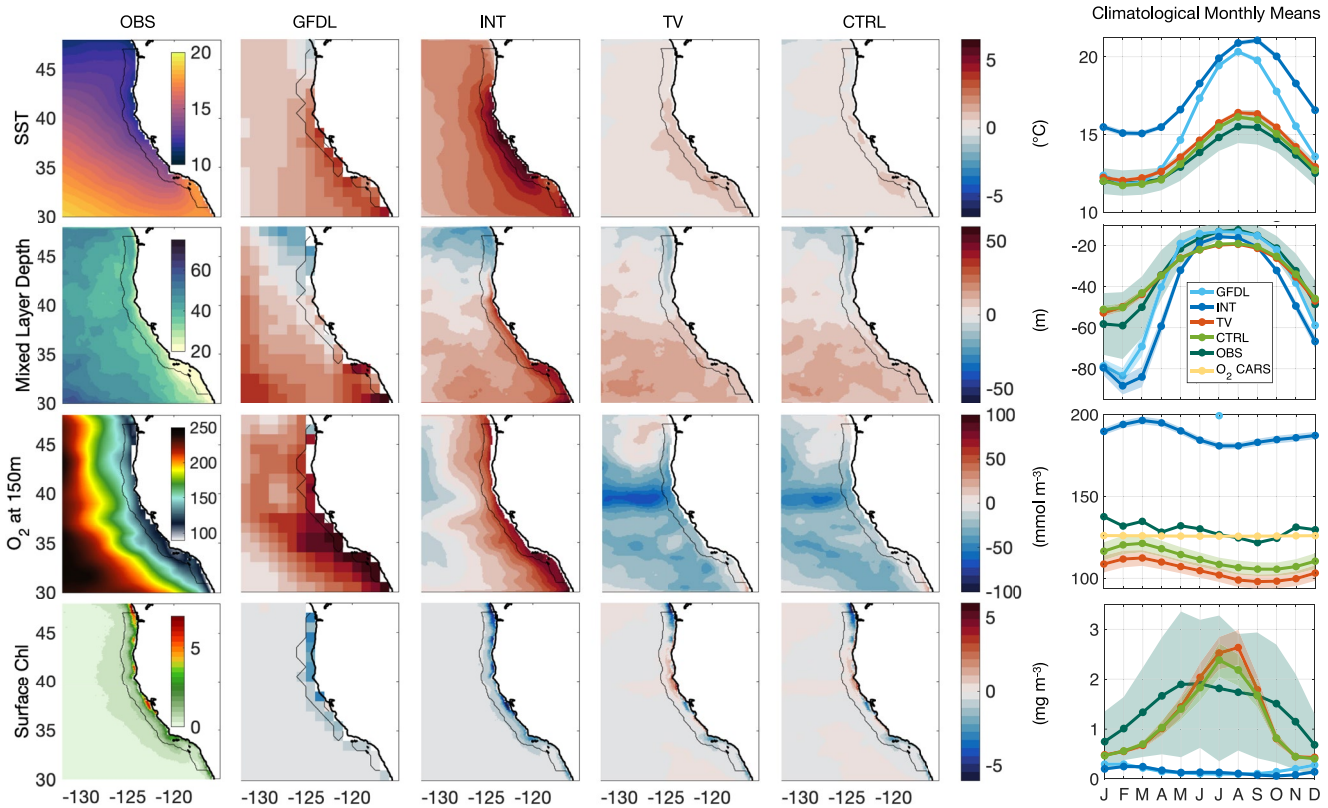


**Figure 3.** Spatial annual mean and bias with respect to observations of ecosystem variables. Rows shown: (top) SST, (second row) MLD, (third row) dissolved oxygen concentration at 150 m, and (bottom row) surface chlorophyll. Columns show: (left) mean historical value of the variables from observations and bias relative to observations for (second column) the GFDL output, (third column) INT, (fourth column) TV, and (fifth column) CTRL. The black/white line represents a 100 km distance from the coast. (right) Historical monthly means of the variables averaged from 100 km to the coast calculated using the original model grid. Shading represents the monthly standard error of the ecosystem variables. For GFDL, oxygen at 150 m is only provided as an annual average. Observational SST data comes from NOAA OISST (1982–2010); MLD from the CCS ROMS reanalysis (1980–2010), subsurface oxygen at 150 m from the CSIRO Atlas of Regional Seas (CARS) climatology and the World Ocean Atlas (1981–2010), and surface chlorophyll from SeaWiFS (2000–2010). Maps showing the spatial annual mean and bias for the subsurface oxygen at 150 m are compared to the CARS climatology. The observed data have been interpolated to the respective model grids for the spatial annual mean comparisons.

bias in the central coastal waters and negative bias in northern and southern coastal regions. Averaging surface chlorophyll for the whole coastal region, both CTRL and TV exhibit a positive bias during the summer months, and a negative bias during the rest of the seasons (fourth row in Figure 3, coastal region in Figure S4 in Supporting Information S1).

### 3.2. Historical Added Value

We also evaluate which downscaled simulation best reproduces the mean historical climate from observations using an Added Value (AV) metric (Equation 3, Dosio et al., 2015). Since the historical period of the SV simulation corresponds to the CTRL run, we only compare the performance of INT and TV with the GFDL output.

INT deteriorates (i.e., negative AV) the representation of SST in the full domain and surface chlorophyll offshore when compared to the GFDL output, particularly in the north (Figure 4). The deterioration of SST in INT seems linked to exacerbation of sensible heat biases (Figure S1 in Supporting Information S1). In contrast, TV improves the representation of SST and surface chlorophyll relative to the GFDL output and INT, except for surface chlorophyll in the north and southwest corner of the domain and in a localized region of the coast near 40°N (first and third rows in Figure 4).

INT also deteriorates the representation of the MLD historical mean compared to the GFDL output for most of the coastal region, except in some localized areas in the north (latitudes >40°N), while offshore, INT improves the

10.1029/2023EA003121



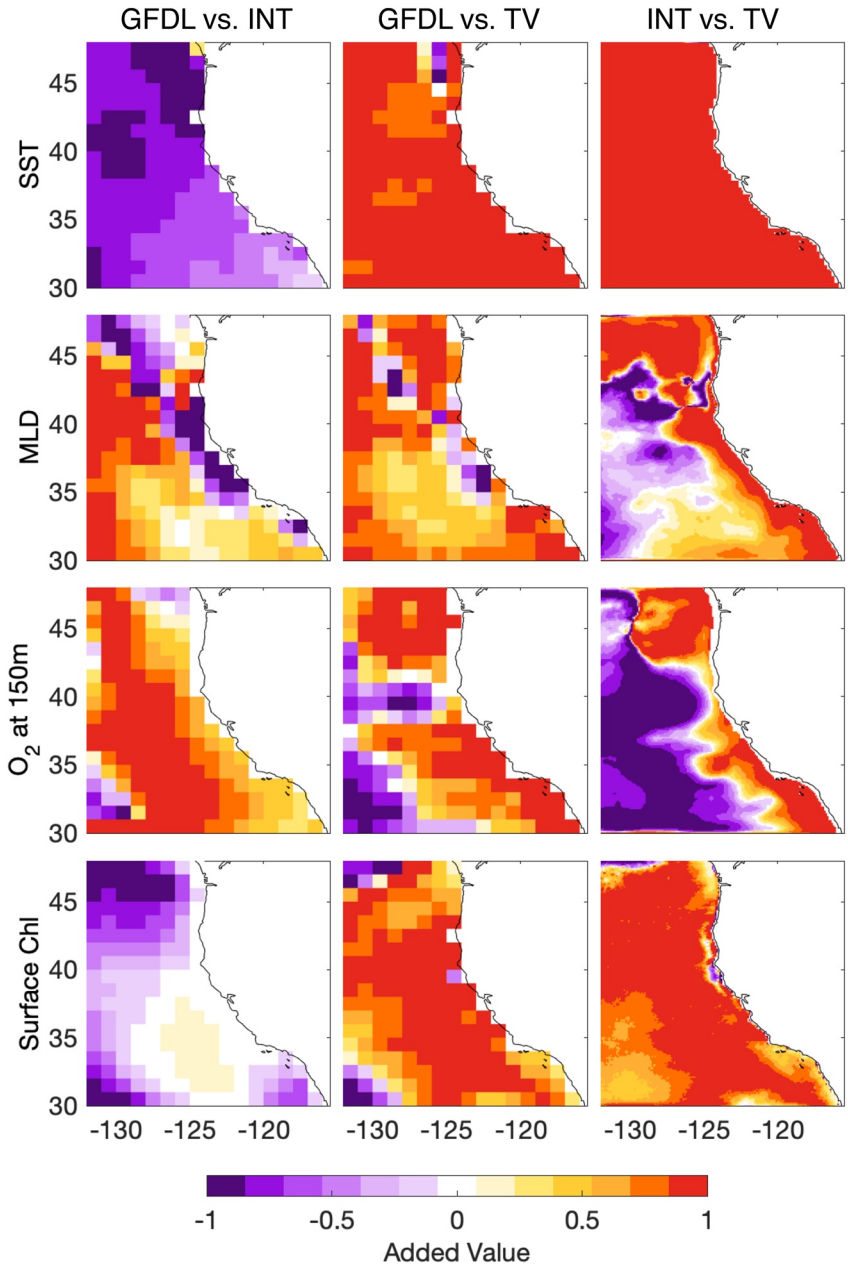


**Figure 4.** (top) Spatial added value for historical climatological mean of SST, (second row) MLD, (third row) subsurface dissolved oxygen at 150 m, and (bottom) surface chlorophyll from (left) INT and (center) TV relative to the GFDL original output, and (right) TV relative to INT. Observations are used as reference. CSIRO CARS climatology is used as reference for subsurface dissolved oxygen.

representation of MLD and subsurface oxygen in most of the domain. In contrast, TV improves the representation of MLD in most of the domain with respect to the GFDL and in the north and along the coast with respect to INT (second and third rows in Figure 4). For subsurface oxygen, TV shows positive AV along the coast with respect to the GFDL and INT simulations, but shows negative AV in the offshore region when compared to INT (third row in Figure 4).

### 3.3. Long-Term Mean and Seasonal Changes

By the end of the century an overall surface warming up to ~2.4°C is projected by all of the models, however strong spatial differences arise between the original GFDL output and the downscaled simulations, especially in

10.1029/2023EA003121



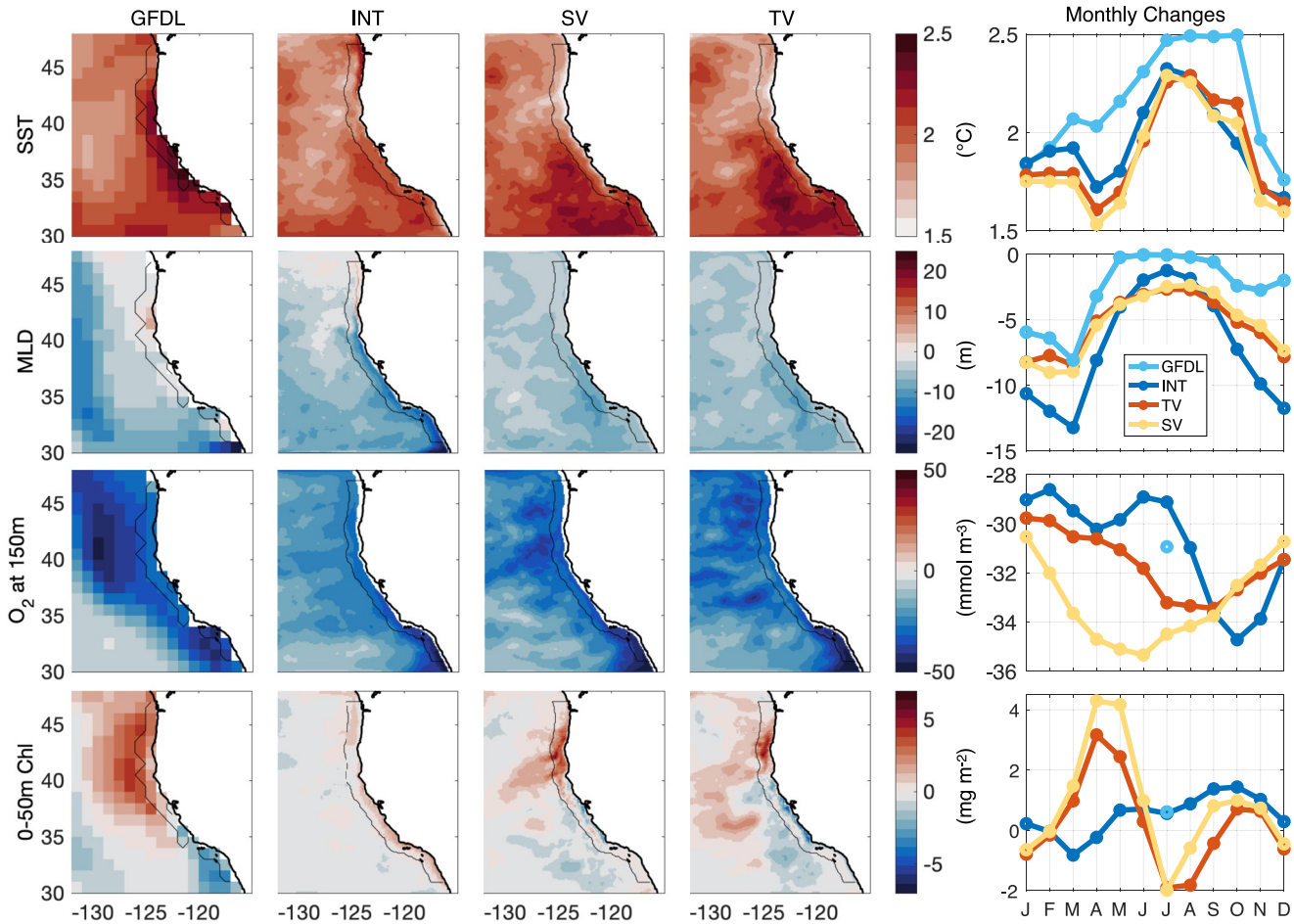


**Figure 5.** Future changes (2070–2100 relative to historical) for the ecosystem variables. Rows shown from top to bottom: SST, MLD, subsurface $O_2$ at 150 m, and integrated chlorophyll from 0 to 50 m for (left) the GFDL output, (second column) INT, (third column) SV, and (fourth column) TV. The black line represents a 100 km distance from the coast. (right) Future monthly changes (2070–2100 relative to historical) averaged from the coast to 100 km offshore. Note that subsurface oxygen at 150 m and integrated chlorophyll from GFDL are only provided as annual averages.

the coastal region (top row Figure 5). In GFDL, the strongest warming occurs in the nearshore region centered between 35 and 45°N. In INT the strongest warming is located in the northern region (>43°N) within ∼50 km of the coast and in the southern coastal CCS. SV and TV project the same spatial changes of SST in the CCS, featuring the strongest warming in the southern CCS, with similar spatial changes to INT, but with larger magnitude of the changes. Both SV and TV project a relatively weak warming ∼1.5°C near the coast that extends offshore in the northern CCS (>40°N) and that can be associated with both a weak projected air temperature increase and an intensification of the upwelling favorable winds in that region (Figure 2). In addition, for SV and TV the peak warming seems to be displaced offshore of the Southern California Bight (SCB, <35°N). Along the coast, the three downscaled simulations project similar seasonal changes in SST, especially during summer, with June and July showing the largest changes in the future; while GFDL projects the highest SST changes from July to September. GFDL exhibits stronger warming than the three downscaled simulations except during winter (top row Figure 5).

A warmer upper-ocean increases stability and may shoal the mixed layer, reducing the source depth of upwelled water and limiting nutrient supply to the surface mixed layer (e.g., Bograd et al., 2023). GFDL projects a ∼10 m shoaling of the MLD in the offshore region while there changes in the coastal region are small except for MLD shoaling (>15 m) near the southern coastal boundary and deepening (∼10 m) between 40 and 43°N (second row in Figure 5). INT shows similar changes of the MLD except for a strong shoaling that follows the coastline from the southern boundary to ∼40°N. SV and TV project weaker shoaling of the MLD with respect to INT,

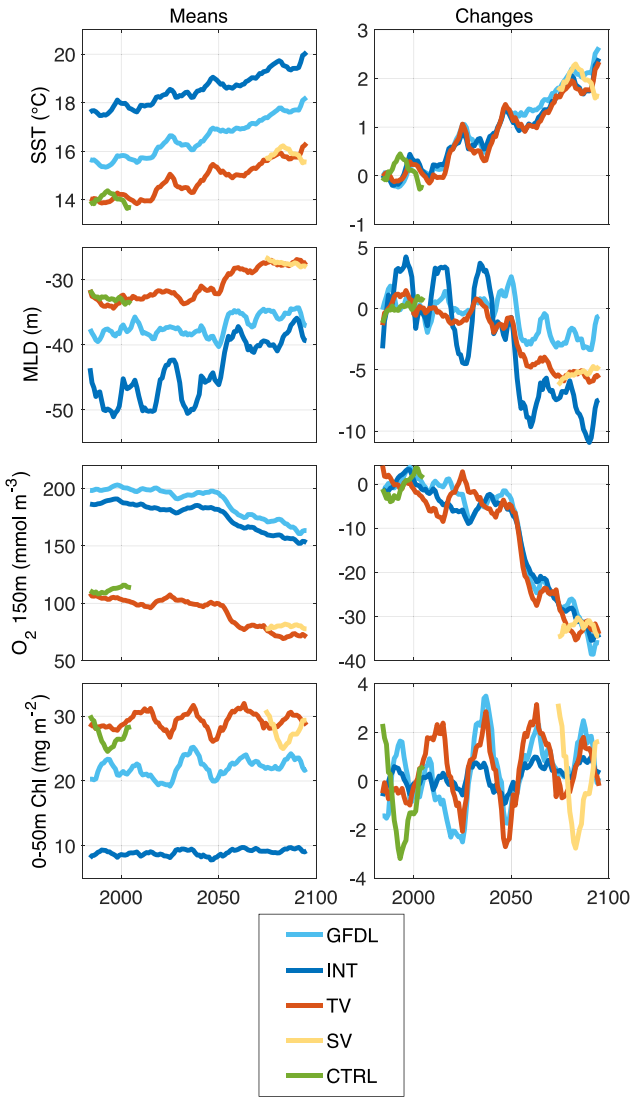


**Figure 6.** Time series of annual means (left) and changes with respect to the historical period (right) averaged from the coast to 100 km offshore of: SST (top), mixed layer depth (second row), subsurface oxygen at 150 m (third row), and vertically integrated chlorophyll from 0 to 50 m (bottom) for the GFDL output (light blue), INT (dark blue), TV (orange), SV (yellow) and the historical CTRL run (green). All the time series have been filtered using a running-mean filter of 10 years.

particularly in the southern CCS. Along the coast, GFDL projects the weakest shoaling of the MLD. INT exhibits the largest MLD shoaling during the winter months, and SV and TV exhibit similar magnitude of future MLD changes over the seasonal cycle. All the models show March as the month with the greatest shoaling of the MLD future change (from 8 to 14 m with respect to their historical period; second row in Figure 5).

The four models project a large-scale decline of subsurface dissolved oxygen at 150 m, and an increase of subsurface nitrate at 150 m, both spatial changes are centered in the offshore waters from the central to northern CCS and in the SCB (third row in Figure 5). Along the coast, the monthly future changes of the subsurface oxygen differ in the three downscaled projections. Maximum decreases are projected during fall in INT, from spring to summer in SV, and from summer to fall in TV (third row in Figure 5). These changes in the subsurface dissolved oxygen mirror the changes in the subsurface nitrate (Figure S5 in Supporting Information S1).

We show the changes of integrated chlorophyll from 0 to 50 m, as a proxy for phytoplankton biomass, (bottom row in Figure 5, and coastal region in Figure S4 in Supporting Information S1). By the end of the century, GFDL output, SV and TV all agree on the sign of the integrated chlorophyll changes. They project an increase of chlorophyll in the northern CCS and a decrease in the Southern California Bight (SCB). However those changes are centered more in the coastal region in both the SV and TV simulations. On the other hand, INT projects a slight increase of chlorophyll only along the shelf from May to November, with no change in the offshore waters in the annual mean. Averaging along the coast, GFDL output projects practically no future changes in the chlorophyll due to a sign compensation along the coast (i.e., increasing/declining in the north/south), while SV and TV both show two peaks of increase in chlorophyll anomalies during the spring and fall months, with the spring increase much greater than the one in fall (bottom row in Figure 5). In SV and TV these increases in chlorophyll are driven by strong future changes in both upwelling favorable winds (Figure 2) and increasing subsurface nutrient concentration (Figure S5 in Supporting Information S1; Pozo Buil et al., 2021).

### 3.4. Time-Varying Changes

To highlight the impact of bias correction methods on interannual variability (as opposed to climatological means), we compare changes in the coastal region for the four ecosystem variables in the downscaled projections (Figure 6). We focus here in a region extending from 100 km offshore to the coast (black/white lines in spatial maps in Figures 1–5). The standardized and percentage of change between the historical and the future period are listed in Table 2.

SST rapidly increases after 2050, with anomalies reaching up to ~2.4°C in GFDL, INT, and TV by the end of the century. Interestingly, end of the century temperature change in SV is ~0.5°C less than the other runs due to the fact that it has interannual variability inherited from the historical period rather than the projection (Figure 6). When averaged over a late-century period instead of looking at the end of century (thereby eliminating the influence of interannual variability), SV is similar to the other runs (Table 2). In INT and TV, the evolution of the SST changes closely follows the GFDL output, resulting in negligible spread among the simulations, except for the SV that follows the evolution of the SST from the CTRL run (first row Figure 6, and Table 2).

The mixed layer is projected to shoal in all simulations, although the magnitude of these changes differs among them, with end-of-century mixed layer depth changes ranging from ~5 m for both the SV and TV up to ~7 m in

**TABLE 2**
*Mean of Change and Percentage Change Between the Historical and the Future Periods*

| | End century - historical mean change, [standardized change], (percentage change) | | | |
|---|---|---|---|---|
| | GFDL-output | INT | SV | TV |
| SST | 2.2°C [2.9] | 1.9°C [2.1] | 1.9°C [2.1] | 1.9°C [2.3] |
| MLD | −2.7 m [-0.2] (−6.9%) | −7.1 m [-0.4] (−15.7%) | −5.3 m [-0.7] (−16.3) | −5.3 m [-0.7] (−16.3) |
| $O_2$ at 150 m | −30.9 mmol $m^{-3}$ [-5.5] (−15.5%) | −30.8 mmol $m^{-3}$ [-4.3] (−16.4%) | −33.2 mmol $m^{-3}$ [-2.2] (−30%) | −31.7 mmol $m^{-3}$ [-4.4] (−30.3%) |
| $NO_3$ at 150 m | 4.5 mmol $m^{-3}$ [4.5] (51.4%) | 4 mmol $m^{-3}$ [2.8] (32.7%) | 3.9 mmol $m^{-3}$ [2] (14.3%) | 3.7 mmol $m^{-3}$ [0.5] (13.4%) |
| Chl 0–50 m | 0.6 mg $m^{-2}$ [0.2] (2.8%) | 0.5 mg $m^{-2}$ [0.2] (5.7%) | 0.8 mg $m^{-2}$ [0.08] (2.9%) | 0.2 mg $m^{-2}$ [0.03] (0.7%) |

*Note.* Changes are computed as the difference between the means of the two reference periods (i.e., 2070–2100 vs. 1980–2010). Negative values in MLD represent shoaling.

INT (second row Figure 6). The change in MLD is even smaller in the GFDL output. Compared to other ecosystem variables, the MLD variability shows the largest spread between the downscaled simulations starting around the mid-century.

Subsurface dissolved oxygen is projected to decrease in all of the simulations, reaching a decline of ∼31.6 mmol $m^{-3}$ in all simulations. However, this decline translates to a lower percentage change in GFDL and INT than in SV and TV (16% vs. 30%) because of positive biases in GFDL and INT historical oxygen concentrations (third row in Figure 6, Table 2, and Figure 3). On the other hand, subsurface nitrate is projected to increase with a change of ∼4 mmol $m^{-3}$ in all simulations by the end of the century (third row in Figure S5 in Supporting Information S1, Table 2). Similar to MLD, the declining (increasing) trend in oxygen (nitrate) is stronger after 2050. In contrast to the rest of the ecosystem variables, the future variability of the subsurface dissolved oxygen in the SV doesn't follow the historical CTRL run. Since the biogeochemical open boundary conditions are climatological, potential subsurface oxygen variability and trends advected into the region (as opposed to generated locally) would be missing in the historical simulation.

By the end of the century, integrated chlorophyll slightly increases in all projections with an average change of ∼3% (∼0.6 mg $m^{-2}$) compared to the historical period (fourth row in Figure 6 and Table 2). Again, the percentage change is higher in GFDL and INT due to historical biases. As highlighted in Figure 5, however, this increase overlies spatially heterogenous patterns that differ between models. In GFDL, SV, TV, the chlorophyll increases in the northern coastal region but decreases in the southern coastal region, so that the net result is a weak increase when averaging over the entire coast (fourth row in Figure 6). In INT the magnitude of the anomalies is smaller but they follow the decadal variability shown in GFDL output. In all the simulations, the integrated chlorophyll is characterized by a strong decadal variability rather than a long-term trend, which is small and spatially heterogeneous.

Overall, the trends and the variability of most of the ecosystem variables closely follow those from the GFDL output, but sometimes with very different magnitudes, variability and spatial patterns (especially for MLD and integrated chlorophyll). The future variability in SV is different from INT and TV because it tracks the historical variability (from the CTRL run) rather than the projected variability. All variables, except the integrated chlorophyll, depict larger trends after 2050 (Table 2). Because of the inherent historical GFDL bias with respect to observations, the evolution of the mean values of the ecosystem variables in INT exhibit an offset compared to the bias-corrected projections (first column in Figure 6).

### 3.5. Changes in Variability

We explore how different bias correction methods applied prior to downscaling represent changes in the variability of ecosystem variables by comparing the interannual standard deviation over the CCS during the historical (1980–2010) and future (2070–2100) periods. To highlight the future changes in variability, we compute the ratio of the standard deviation in the future relative to the historical period (Figure 7; historical standard deviations are shown in Figure S6 in Supporting Information S1).

For the historical period, the SST standard deviation in GFDL is lower compared to the CTRL and the downscaled simulations (first row in Figure S3 in Supporting Information S1). INT exhibits the largest SST variability

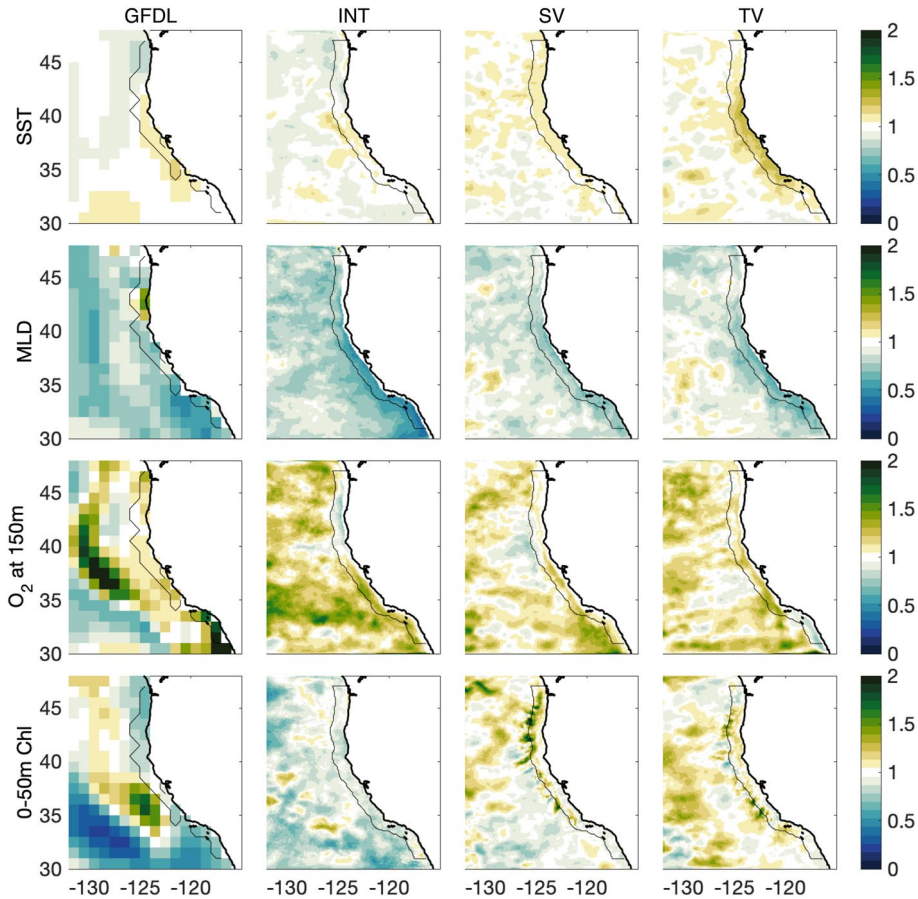


**Figure 7.** Ratio between future (2070–2100) and historical (1980–2010) standard deviation for the ecosystem variables. Rows shown from top to bottom: SST, MLD, subsurface $O_2$ at 150 m, and integrated chlorophyll from 0 to 50 m for the GFDL output (left), INT (second column), SV (third column), and TV (fourth column). The black line represents a 100 km distance from the coast.

from 40 to 45°N along the coast. CTRL and TV exhibit similar spatial patterns of SST variability, with slightly larger magnitude in the central coast in the CTRL run (first row in Figure S6 in Supporting Information S1). The future/historical ratio of SST standard deviation increases along the coast between ~33 and 40°N in GFDL, INT and TV, with TV showing the largest increase (first row in Figure 7). The ratio of the SST standard deviation in SV is close to one over much of the CCS domain.

The four simulations exhibit strong MLD variability in the southwestern corner of the CCS domain during the historical period, with GFDL showing the highest values (second row in Figure S6 in Supporting Information S1). GFDL also exhibits high MLD variability in the SCB. INT exhibits high MLD variability across the domain and higher values along the central coast compared to the other simulations. CTRL and TV show a similar spatial pattern and magnitude of historical MLD variability (second row in Figure S3 in Supporting Information S1). During the future period, the four simulations show a reduction of MLD variability along the coastal region and in the SCB (second row in Figure 7), the same regions where the MLD is projected to shoal (second row in Figure 5). GFDL shows an increase of the variability in the coastal region between 40 and 45°N, where it is projected to get deeper.

GFDL exhibits lower magnitude and different spatial pattern of the subsurface oxygen standard deviation compared to the ROMS simulations during the historical period (third row in Figure S6 in Supporting Information S1). CTRL and TV exhibit similar high values and spatial patterns of subsurface oxygen variability in the offshore waters. INT also exhibits this spatial pattern but with lower magnitude (third row in Figure S6 in Supporting Information S1). GFDL exhibits the largest increase in standard deviation along the coast and in a distinct band of the offshore central region, while the downscaled simulations show an overall enhancement of variability in most regions but with much less structure (third row in Figure 7)

10.1029/2023EA003121

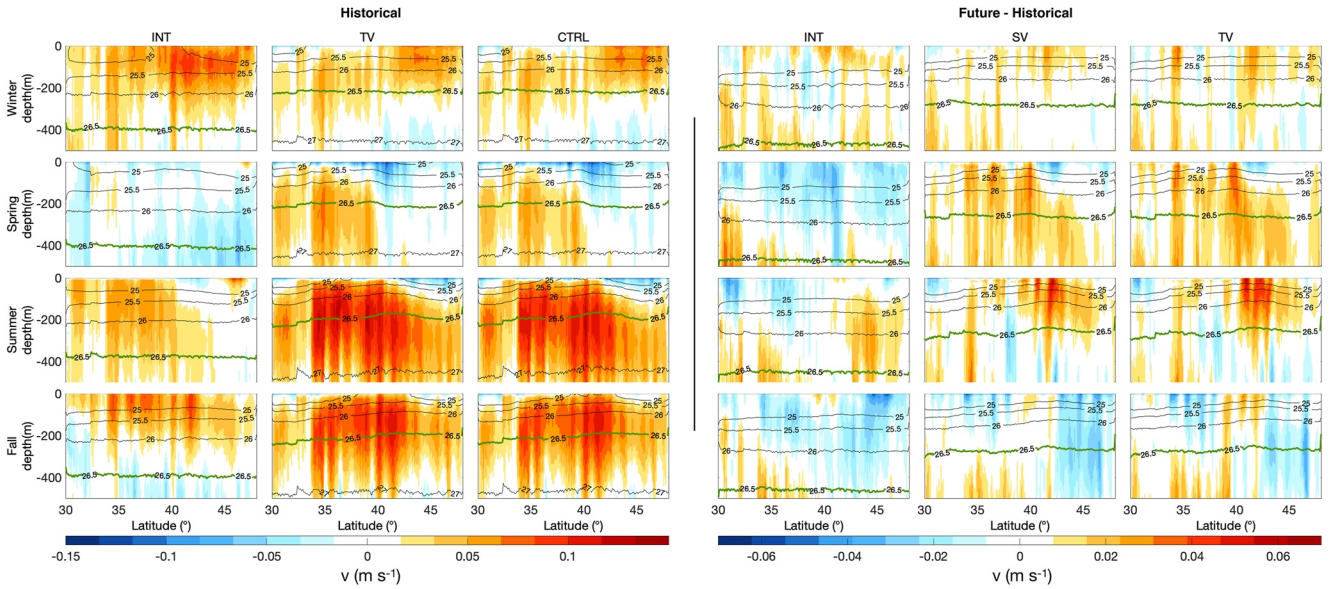


**Figure 8.** Historical (left panels) and future changes (right panels) relative to historical (2070–2100 vs. 1980–2010), of seasonal averages of meridional velocity (shading, positive northward) as a function of latitude along the 500 m isobath for the INT, SV, and TV simulations. The CTRL run represents the historical period of SV. Isopycnal layers are shown in black contours. The green contour corresponds to the isopycnal layer 26.5, representing the core of the CU. For the panels on the right, the contours represent the future mean (2070–2100) of the selected isopycnal levels.

The four simulations exhibit a similar pattern of the integrated chlorophyll historical standard deviation, with high values along the coast between 35 and 45°N (fourth row in Figure S6 in Supporting Information S1), though the magnitude of the historical standard deviation is relatively higher in CTRL and TV compared to GFDL and INT (fourth row in Figure S3 in Supporting Information S1). GFDL exhibits a future enhancement of the integrated chlorophyll variability from ~33 to 45°N in an offshore band, similar to the pattern for oxygen, while the rest of the domain exhibits reduced variability. The downscaled models all show less pronounced changes in variability. An overall reduction of integrated chlorophyll variability is seen along the coast in INT, while SV and TV exhibit similar increases along the coast (fourth row in Figure 7).

### 3.6. Representation of the California Undercurrent and Water Mass Properties

Analyses in the preceding sections highlight how the bias correction approach applied prior to downscaling can influence projected changes in the mean and variability of the ocean state. To further examine how downscaling choices can influence the circulation itself, we present a more detailed case study of the California Undercurrent - a key dynamical feature off the North American west coast that is often not well resolved in ESMs.

The main climatological features and seasonality of the CU are similar in both TV and CTRL (second and third column in Figures 8 and 9). During the historical period, both simulations show the core of the CU transporting the Pacific Equatorial Water (PEW) into the CCS (Bograd et al., 2015; Nam et al., 2015), and characterized by velocities >0.1 m $s^{-1}$, density of ~26.5 kg $m^{-3}$ (Pierce et al., 2000; Rudnick et al., 2017; Zaba et al., 2021), elevated temperatures and salinities (i.e., spicy water), and reduced oxygen content (first column in Figures S7 and S8 in Supporting Information S1 and Figure 9). While these features from the CTRL and TV are comparable to results from previous modeling studies (e.g., Connolly et al., 2014; Durski et al., 2017), INT depicts a less accurate representation of the CU (first column in Figures 8 and 9) compared to CTRL. Although this latter simulation (INT) is able to capture the intensification of the CU in summer, the CU is weaker and the position of its core is misplaced along the slope compared to the CTRL run. The CU has a surface signature that extends along all latitudes during fall and winter, but it undergoes an extreme weakening during spring, with its signature concentrated only in the southern CCS (up to 35°N) in INT. In addition, the core of the CU in INT is less dense (~26 kg $m^{-3}$ in summer) while the 26.5 isopycnal layer is found deeper in INT compared to CTRL and TV (~400 vs. ~200 m).

By the end of the century, SV and TV project a similar subsurface intensification of the CU in spring over most latitudes, a surface intensification in summer, and a weakening in the northern latitudes in fall (fifth and sixth columns in Figure 8). However, INT projects an intensification of the CU at ~400 m depth in spring, summer, and

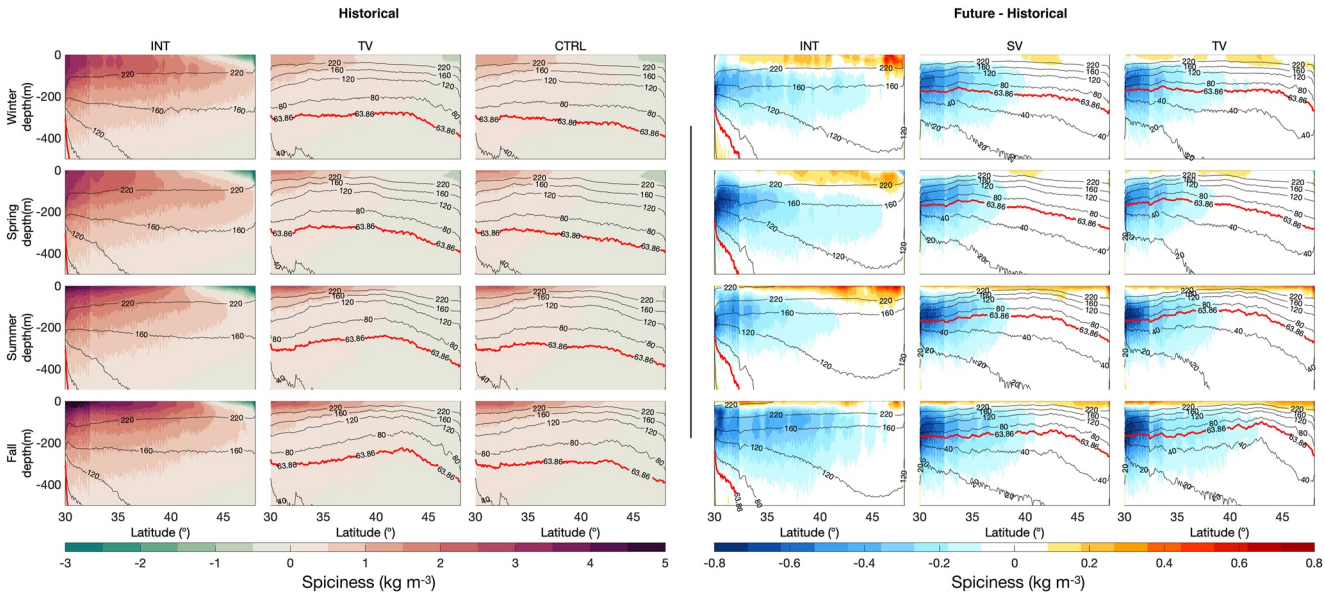


**Figure 9.** Historical (left panels) and future changes (right panels) relative to historical (2070–2100 vs. 1980–2010) of seasonal averages of spiciness (shading) as a function of latitude along the 500 m isobath for INT, SV, and TV. The CTRL run represents the historical period of SV. Constant dissolved oxygen concentration layers are shown in black contours. The red contour corresponds to the hypoxic boundary layer (63.86 mmol $m^{-3}$ or 1.43 ml $l^{-1}$). For the panels on the right, the contours represent the future mean (2070–2100) of dissolved oxygen concentration.

fall, with a slight intensification between 40 and 45°N in summer, and surface weakening in fall (fourth column in Figure 8). In all the downscaled simulations, the core of the CU is projected to deepen especially during fall and also for winter and spring in INT (fourth to sixth columns in Figure 8).

In summer, the CU transports spicier equatorial source waters northward. The CU has a signature of spicy waters from the surface to ∼200 m depth. In spring, the surface flow is primarily equatorward (Figure 8) transporting mintier (i.e., colder and fresher) subarctic source waters with higher oxygen concentration into the CCS (second and third column in Figure 9). This can be noted by the southward retraction of spicy near-surface waters in spring (second row, second and third column in Figure 9). Compared to CTRL and TV, INT highlights spicier waters along most of the slope and mintier waters concentrated at the surface near the northern boundary (first column Figure 9). These differences in the magnitude and spatial distribution of the spiciness among the simulations occur because INT produces warmer and denser waters along the slope, with saltier (fresher) waters at the southern (northern) boundary when compared to CTRL during the historical period (Figures S7 and S8 in Supporting Information S1). The CU also transports low oxygen content waters from the equator. In CTRL and TV, the depth of the hypoxic boundary (defined here as 63.86 mmol $m^{-3}$) varies between 300 and 400 m along the slope, while in INT the content of oxygen is higher in the subsurface, deepening the hypoxic boundary layer along the slope (Figure 9).

By the end of the century, the three downscaled simulations project similar spatial changes of spiciness, but the magnitude of these changes is different (fourth to sixth columns in Figure 9). The CU is projected to transport less spicy (colder and fresher) waters from the equator, extending up to 42°N in the fall in SV and TV and further north in INT. These future changes in the CU spiciness have a larger magnitude near the southern boundary in summer and fall in both SV and TV, but a larger magnitude in spring in INT (fourth to sixth columns in Figure 9). The three downscaled simulations project similar changes in temperature and salinity, but the magnitudes and their spatial distributions are different (fourth to sixth columns in Figures S7 and S8 in Supporting Information S1). In SV and TV, salinity changes are mainly located near ∼150 m depth, while in INT these changes are shallower.

Future waters over the slope (from the surface to 50 m depth) are projected to become spicier in the downscaled simulations because of the surface warming. In INT, these changes are larger and deeper (from the surface to ∼100 m), especially near the northern boundary. In addition, the hypoxic boundary is projected to become shallower along the slope (fourth to sixth columns in Figure 9), which has also been shown in previous studies (e.g.,

10.1029/2023EA003121



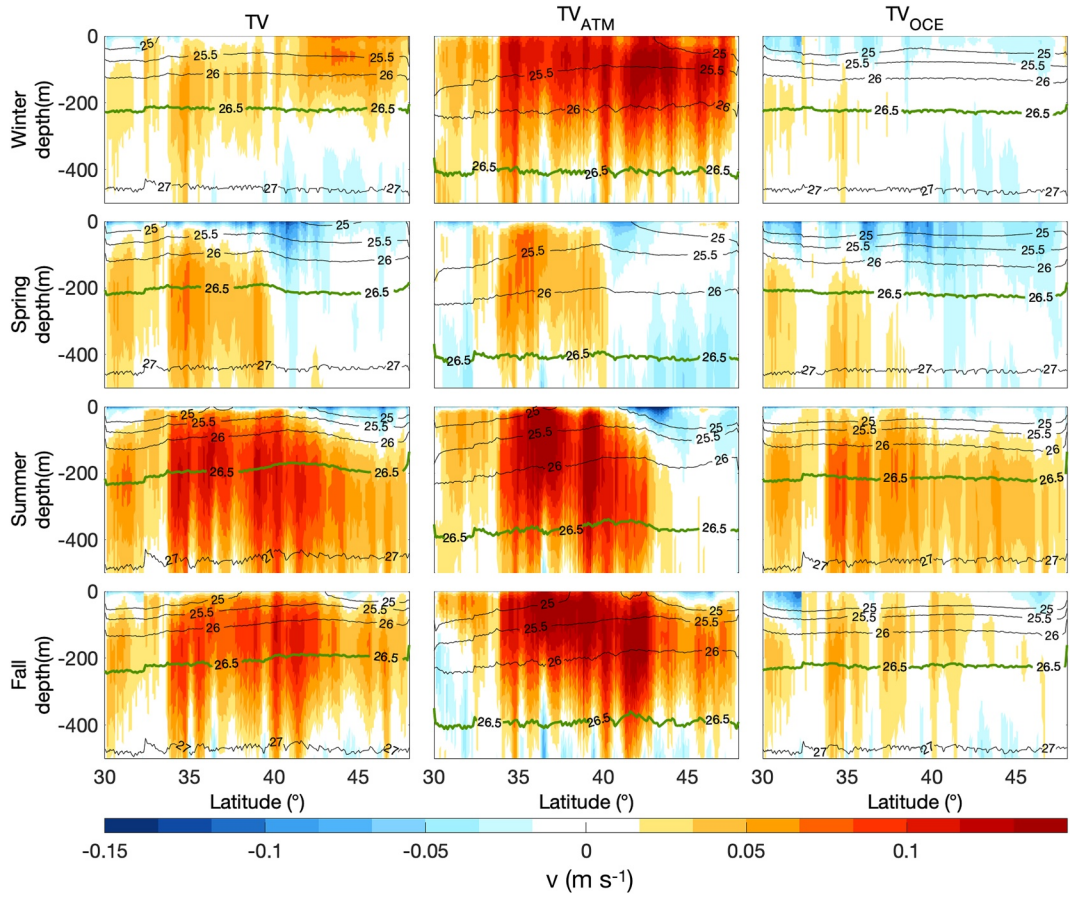


**Figure 10.** Historical seasonal averages of meridional velocity and density as a function of latitude along the 500 m isobath for the TV (left), $TV_{ATM}$ (second column), $TV_{OCE}$ (third column) simulations. Isopycnal layers are shown in black contours. The green contour corresponds to the isopycnal level 26.5, representing the core of the CU.

Dussin et al., 2019; Pozo Buil et al., 2021). While SV and TV project hypoxic subsurface waters deeper than ~200 m and the hypoxic boundary shoaling up ~100 m at some latitudes, INT projects hypoxic waters only near the southern boundary (up to 33°N) and a deeper hypoxic boundary, below ~300 m of depth (fourth to sixth columns in Figure 9).

### 3.6.1. CU Sensitivity to Bias Corrected Boundary Conditions

Given the sensitivity of the CU dynamics to downscaling method, we explore the relative influences of atmospheric and ocean forcing on the regional simulation by conducting two additional sensitivity experiments: (a) bias correcting only the local atmospheric forcing and directly interpolating the oceanic open boundary conditions from the GFDL output ($TV_{ATM}$) and, (b) bias correcting only the remote oceanic open boundary conditions and directly interpolating the atmospheric forcing from the GFDL output ($TV_{OCE}$, Table 1).

Bias correcting only the atmospheric forcing ($TV_{ATM}$, second column in Figure 10) reproduces the seasonal variability of the CU, but generates a stronger CU (i.e., increases the magnitude of its velocity core), especially from summer to winter, while in spring the core of the CU is shallower from 35 to 40°N and weaker in the southern latitudes (30–34°N). In addition, the CU transports less dense (~26 kg m$^{-3}$) water in the $TV_{ATM}$ simulation compared to the CTRL (~26.5 kg m$^{-3}$) run, and the density profile along the slope is similar to the INT simulation (first column in Figure 8).

On the other hand, bias correcting only the ocean boundary conditions ($TV_{OCE}$, third column in Figure 10) reproduces the density profile along the slope similar to the CTRL simulation because the temperature and salinity GFDL biases are corrected prior to downscaling. However, $TV_{OCE}$ generates a weaker CU that is evident in the four seasons compared to the CTRL simulation. This enhanced weakening of the CU occurs during winter, and

the surface circulation over the slope becomes equatorward in both winter and spring (third column in Figure 10). The weaker CU in the $TV_{OCE}$ simulation may be a result of inheriting a weaker windstress from the GFDL output compared to the CTRL simulation (second row in Figure 1).

## 4. Summary and Discussion

Here we have examined the future response of key ecosystem variables for the CCS using the GFDL-ESM2M and two bias correction techniques applied prior to dynamical downscaling: (a) a traditional interpolation of an ESM forcing to the ocean model grid with no bias correction; (b) a "seasonally-varying" delta method that included the seasonal dependence of future climate change (Alexander et al., 2019); and (c) a "time-varying" delta method that included the seasonal and interannual variability of the ESM (Pozo Buil et al., 2021).

Overall, the four simulations project future surface warming, a shoaling of the mixed layer depth, a decline in subsurface dissolved oxygen, an increase in subsurface nitrate, and a modest increase in chlorophyll. Although the sign of changes agrees for most variables among the four simulations, the spatial patterns and magnitudes of the projected changes differ, with SV and TV showing mean spatial and seasonal changes similar to each other but different from those in the GFDL and INT runs.

In INT and TV, most of the ecosystem variables inherit variability from the GFDL projection, with changes in most of the ecosystem variables being larger after ~2050. In contrast, SV has future variability that, by construction, tracks the historical variability rather than the projected variability. In all the projections, the vertically integrated chlorophyll exhibits a strong decadal variability. Using shorter time-slices to define the future period could lead to false attributions of this signal to anthropogenic climate change instead of natural climate variability (e.g., Deser et al., 2012). Projecting for the full transient period or longer time-scales (>30 years) are recommended in downscaling protocols (Drenkard et al., 2021).

We have used two delta methods to dynamically downscale the GFDL output: the seasonally- and time-varying delta methods. Both methods adjusted the mean historical bias of the atmospheric and the oceanic forcing from the global climate model output, retained the high-frequency spatiotemporal variability (i.e., daily variability and fine-scale spatial variability of the historical climate), and overall produced similar climatological future mean, seasonal changes, and changes in the variance of the ecosystem variables. In the seasonally-varying delta method, since the future temporal variabilities in the boundary condition forcings (except for the mean future changes) are obtained from those in the CTRL run, the relationships between variables in the CTRL run (historical climate) are likely to be maintained in the future. Thus, the seasonally-varying delta method is not well suited for the projection of changes in interannual and decadal variability (e.g., Alexander et al., 2019; Shin & Alexander, 2020; Xu et al., 2019). Furthermore, while the seasonally-varying delta method limits the future years of the projections to the length of the historical period, the time-varying delta method is able to resolve the full climate evolution and capture changes in interannual variability, including potential nonlinear impacts that would be missed when the transient response is excluded (Pozo Buil et al., 2021).

The perception that "higher resolution is better" usually leads to the assumption that downscaling ESMs increases the value of these projections; however, depending on the bias correction method, this is not always the case. Here we have shown how the non-bias corrected dynamical downscaling method (INT) still propagates the historical bias from the GFDL forcing across the open boundaries of the forced domain and that this bias can even get amplified (Figure 3 and, e.g., Hall, 2014). In contrast, the time-varying delta method (TV) is able to reproduce similar biases with respect to the observations as the CTRL simulation, verifying its effectiveness in reducing the historical GFDL bias. Compared to the GFDL output, both the INT and TV dynamically downscaled methods introduce added value as a result of resolving features on regional scale even when these results are averaged to the coarse grid scale in the GFDL (e.g., Wang et al., 2015), with the exception of SST and coastal surface Chl in INT. When comparing the non-bias corrected method (or direct interpolation) and the time-varying delta method to each other during the historical period, the time-varying-delta method performs better along the coast and also improves the representation of the seasonal cycle of the ecosystem's variables (Figure 4).

Because of its role in the CCS dynamics and potential contribution to the source of upwelled waters (Bograd et al., 2015; Lynn & Simpson, 1987), an accurate representation of the CU is necessary when investigating future changes in the CCS ecosystem. Our results also showed the added value of bias correcting the GFDL forcing for accurately reproducing the mean alongshore circulation and the climatological features and seasonality of

the California Undercurrent. By the end of the century, both SV and TV projected an increase of transport in CU but a reduction in spiciness. However, future changes in CU differ between INT and the two bias corrected downscaled simulations.

Additional sensitivity experiments highlighted the importance of bias correcting both the atmospheric and ocean boundary conditions when downscaling ESMs. Bias correcting only the atmospheric forcing ($TV_{ATM}$) reproduces the seasonal variability of the CU but generates a stronger CU (i.e., increases the magnitude of its velocity core) that transports less dense water (~26 kg $m^{-3}$). The vertical density structure in $TV_{ATM}$ could be due to warmer and saltier waters inherited from the GFDL simulation (i.e., INT compared to the CTRL simulation, Figures S7 and S8 in Supporting Information S1). While bias correcting only the ocean boundary conditions ($TV_{OCE}$) reproduces the density profile along the slope but generates a weaker CU (Figure 10). The weakening of the CU in $TV_{OCE}$ could be associated with the weaker meridional wind stress inherited from the GFDL output (second row in Figure 1), which weakens the alongshore pressure gradient driving a weaker CU compared to $TV_{ATM}$ and TV. In TV, the atmospheric and oceanic forcing are both bias corrected, compensating the weaker CU, the vertical density distribution, and representing a more accurate CU when comparing to the CTRL simulation. Alongshore pressure gradient forcing and vertical stratification have been shown to be important factors driving the structure of the CU and its temporal variability (Connolly et al., 2014; Hickey et al., 2006).

There are several continuations of this work that should be explored. First, ESMs belonging to the CMIP5 archive only included annually averaged BGC output, so future dynamical downscaling work would benefit from the new CMIP6 archive that provides biogeochemical variables at monthly resolution. Second, we evaluated combined statistical and dynamical downscaling methods that only correct the mean climatological historical bias of an ESM; future work should include other combinations of downscaling methods to correct other statistics, like the variance and frequency of extreme events.

## 5. Conclusion

Our different downscaled climate projections show that when forcing regional ocean models with ESMs, bias correcting the ESM forcing prior to downscaling is key to reducing the historical ESM bias and resolving coastal processes critical to projecting ecosystem changes. Not bias correcting the ESM forcing can lead to the amplification of the ESM historical bias and the misrepresentation of coastal circulation dynamics and water masses of the CCS. The two bias correction methods, seasonally- and time-varying delta, adjusted the mean historical bias of the forcing from the global climate model output and retained the high-frequency spatiotemporal variability. We suggest the use of the seasonally-varying delta method when research questions are focused on the long-term changes (e.g., end-of century vs. historical), with the caveat that the future years of the projections would be limited to the length of the historical period. Since the seasonally-varying delta method inherits the historical variability, this method is not well suited for the projection of the changes in interannual and decadal variability if the processes driving variability substantially change over time. The seasonal-varying delta method allows for shorter simulations (i.e., less computer time) and may better represent the mean change if there is substantial low frequency variability. This suggests that the period in SV (or any fixed delta method) should be long enough to average out decadal variability and/or an ensemble of simulations should be performed. On the other hand, the time-varying delta method is able to resolve the full climate evolution and capture changes in interannual variability, including potential nonlinear impacts that would be missed when the transient response is excluded. When coupling these ocean and biogeochemical simulations to ecological models, these differences in the characteristics of downscaled simulations will have important implications for higher trophic levels (Smith et al., 2023) and should be carefully considered in the experimental design.

## Data Availability Statement

TV projection is available at the NOAA Climate Change Portal https://psl.noaa.gov/ipcc/ccs/ and at NOAA ERDDAP https://oceanview.pfeg.noaa.gov/erddap/search/index.html?page=1&itemsPerPage=1000&searchFor=CCS%20ROMS. Outputs from the historical control run, TV, INT, and SV from this work are freely and openly available and through dryad at: https://doi.org/10.5061/dryad.t1g1jwt8c (Pozo Buil, 2023. Data from Evaluation of different bias correction methods for dynamical downscaled future projections of the California Current Upwelling System [Dataset]).

**Acknowledgments**
Funding was provided by the National Oceanic and Atmospheric Administration's Modeling, Analysis, Predictions and Projections Program (NA20OAR4310447). Matlab code to compute spiciness, is available at http://www.teos-10.org/software/. We thank the CalCOFI program (https://calcofi.org/) and the CSIRO Atlas of Regional Seas (CARS2009, http://www.cmar.csiro.au/cars) for making their data available thorugh their websites.The authors thank Charles A. Stock for helpful comments on an earlier version of the manuscript.

## References

Alexander, M. A., Shin, S.-i., Scott, J. D., Curchitser, E., & Stock, C. (2019). The response of the Northwest Atlantic Ocean to climate change. *Journal of Climate*, *33*(2), 405–428. https://doi.org/10.1175/jcli-d-19-0117.1

Anderson, J. L. (2004). The new GFDL global atmosphere and land model AM2–LM2: Evaluation with prescribed SST simulations. *Journal of Climate*, *17*, 4641–4673.

Arellano, B., & Rivas, D. (2019). Coastal upwelling will intensify along the Baja California coast under climate change by mid-21st century: Insights from a GCM-nested physical-NPZD coupled numerical ocean model. *Journal of Marine Systems*, *199*, 103207. https://doi.org/10.1016/j.jmarsys.2019.103207

Atlas, R., Hoffman, R. N., Ardizzone, J., Leidner, S. M., Jusem, J. C., Smith, D. K., & Gombos, D. (2011). A cross-calibrated, multiplatform ocean surface wind velocity product for meteorological and oceanographic applications. *Bulletin of the American Meteorological Society*, *92*(2), 157–174. https://doi.org/10.1175/2010bams2946.1

Auad, G., Miller, A., & Di Lorenzo, E. (2006). Long-term forecast of oceanic conditions off California and their biological implications. *Journal of Geophysical Research*, *111*(C9). https://doi.org/10.1029/2005jc003219

Bograd, S. J., Buil, M. P., Lorenzo, E. D., Castro, C. G., Schroeder, I. D., Goericke, R., et al. (2015). Changes in source waters to the southern California Bight. *Deep Sea Research Part II: Topical Studies in Oceanography*, *112*, 42–52. https://doi.org/10.1016/j.dsr2.2014.04.009

Bograd, S. J., Jacox, M. G., Hazen, E. L., Lovecchio, E., Montes, I., Pozo Buil, M., et al. (2023). Climate change impacts on eastern boundary upwelling systems. *Annual Review of Marine Science*, *15*(1), 303–328. https://doi.org/10.1146/annurev-marine-032122-021945

Bruyère, C. L., Done, J. M., Holland, G. J., & Fredrick, S. (2014). Bias corrections of global models for regional climate simulations of high-impact weather. *Climate Dynamics*, *43*(7–8), 1847–1856. https://doi.org/10.1007/s00382-013-2011-6

Cambon, G., Goubanova, K., Marchesiello, P., Dewitte, B., Illig, S., & Echevin, V. (2013). Assessing the impact of downscaled winds on a regional ocean model simulation of the Humboldt system. *Ocean Modelling*, *65*, 11–24. https://doi.org/10.1016/j.ocemod.2013.01.007

Capet, X. J., Marchesiello, P., & McWilliams, J. C. (2004). Upwelling response to coastal wind profiles. *Geophysical Research Letters*, *31*(13). https://doi.org/10.1029/2004gl020123

Carton, J. A., & Giese, B. S. (2008). A reanalysis of Ocean climate using Simple Ocean Data assimilation (SODA). *Monthly Weather Review*, *136*(8), 2999–3017. https://doi.org/10.1175/2007mwr1978.1

Checkley, D. M., & Barth, J. A. (2009). Patterns and processes in the California current system. *Progress in Oceanography*, *83*(1–4), 49–64. https://doi.org/10.1016/j.pocean.2009.07.028

Cheresh, J., & Fiechter, J. (2020). Physical and biogeochemical drivers of alongshore pH and oxygen variability in the California Current System. *Geophysical Research Letters*, *47*(19). https://doi.org/10.1029/2020gl089553

Cheung, W. W. L., Frölicher, T. L., Asch, R. G., Jones, M. C., Pinsky, M. L., Reygondeau, G., et al. (2016). Building confidence in projections of the responses of living marine resources to climate change. *fsv250*, *73*, 1283–1296. https://doi.org/10.1093/icesjms/fsv250

Chhak, K., & Di Lorenzo, E. (2007). Decadal variations in the California Current upwelling cells. *Geophysical Research Letters*, *34*(14). https://doi.org/10.1029/2007gl030203

Connolly, T. P., Hickey, B. M., Shulman, I., & Thomson, R. E. (2014). Coastal trapped waves, alongshore pressure gradients, and the California undercurrent. *Journal of Physical Oceanography*, *44*(1), 319–342. https://doi.org/10.1175/jpo-d-13-095.1

Deser, C., Knutti, R., Solomon, S., & Phillips, A. S. (2012). Communication of the role of natural variability in future North American climate. *Nature Climate Change*, *2*(11), 775–779. https://doi.org/10.1038/nclimate1562

Dosio, A., Panitz, H.-J., Schubert-Frisius, M., & Lüthi, D. (2015). Dynamical downscaling of CMIP5 global circulation models over CORDEX-Africa with COSMO-CLM: Evaluation over the present climate and analysis of the added value. *Climate Dynamics*, *44*(9–10), 2637–2661. https://doi.org/10.1007/s00382-014-2262-x

Drenkard, E. J., Stock, C., Ross, A. C., Dixon, K. W., Adcroft, A., Alexander, M., et al. (2021). Next-generation regional ocean projections for living marine resource management in a changing climate. *ICES Journal of Marine Science*, *78*(6), 1969–1987. https://doi.org/10.1093/icesjms/fsab100

Dunn, J. R., & Ridgway, K. R. (2002). Mapping ocean properties in regions of complex topography. *Deep Sea Research Part I: Oceanographic Research Papers*, *49*(3), 591–604. https://doi.org/10.1016/S0967-0637(01)00069-3

Dunne, J. P., John, J. G., Adcroft, A. J., Griffies, S. M., Hallberg, R. W., Shevliakova, E., et al. (2012). GFDL's ESM2 global coupled climate–carbon earth system models. Part I: Physical formulation and baseline simulation characteristics. *Journal of Climate*, *25*(19), 6646–6665. https://doi.org/10.1175/jcli-d-11-00560.1

Dunne, J. P., John, J. G., Shevliakova, E., Stouffer, R. J., Krasting, J. P., Malyshev, S. L., et al. (2013). GFDL's ESM2 global coupled climate–carbon earth system models. Part II: Carbon system formulation and baseline simulation characteristics. *Journal of Climate*, *26*(7), 2247–2267. https://doi.org/10.1175/jcli-d-12-00150.1

Durski, S. M., Barth, J. A., McWilliams, J. C., Frenzel, H., & Deutsch, C. (2017). The influence of variable slope-water characteristics on dissolved oxygen levels in the northern California current system. *Journal of Geophysical Research: Oceans*, *122*(9), 7674–7697. https://doi.org/10.1002/2017jc013089

Dussin, R., Curchitser, E. N., Stock, C. A., & Van Oostende, N. (2019). Biogeochemical drivers of changing hypoxia in the California Current Ecosystem. *Deep Sea Research Part II: Topical Studies in Oceanography*, *169–170*, 104590. https://doi.org/10.1016/j.dsr2.2019.05.013

Echevin, V., Gévaudan, M., Espinoza-Morriberón, D., Tam, J., Aumont, O., Gutierrez, D., & Colas, F. (2020). Physical and biogeochemical impacts of RCP8.5 scenario in the Peru upwelling system. *Biogeosciences*, *17*(12), 3317–3341. https://doi.org/10.5194/bg-17-3317-2020

Echevin, V., Goubanova, K., Belmadani, A., & Dewitte, B. (2012). Sensitivity of the Humboldt current system to global warming: A downscaling experiment of the IPSL-CM4 model. *Climate Dynamics*, *38*(3–4), 761–774. https://doi.org/10.1007/s00382-011-1085-2

Fairall, C. W., Bradley, E. F., Godfrey, J. S., Wick, G. A., Edson, J. B., & Young, G. S. (1996b). Cool-skin and warm-layer effects on sea surface temperature. *Journal of Geophysical Research*, *101*(C1), 1295–1308. https://doi.org/10.1029/95jc03190

Fairall, C. W., Bradley, E. F., Rogers, D. P., Edson, J. B., & Young, G. S. (1996). Bulk parameterization of air-sea fluxes for tropical ocean-global atmosphere coupled-ocean atmosphere response experiment. *Journal of Geophysical Research*, *101*(C2), 3747–3764. https://doi.org/10.1029/95jc03205

Fiechter, J., Curchitser, E. N., Edwards, C. A., Chai, F., Goebel, N. L., & Chavez, F. P. (2014). Air-sea $CO_2$ fluxes in the California Current: Impacts of model resolution and coastal topography. *Global Biogeochemical Cycles*, *28*(4), 371–385. https://doi.org/10.1002/2013gb004683

Fiechter, J., Edwards, C. A., & Moore, A. M. (2018). Wind, circulation, and topographic effects on alongshore phytoplankton variability in the California current. *Geophysical Research Letters*, *45*(7), 3238–3245. https://doi.org/10.1002/2017gl076839

Franco, A. C., Gruber, N., Frölicher, T. L., & Kropuenske Artman, L. (2018). Contrasting impact of future CO2 emission scenarios on the extent of CaCO3 mineral undersaturation in the Humboldt current system. *Journal of Geophysical Research: Oceans*, *123*(3), 2018–2036. https://doi.org/10.1002/2018jc013857

Frölicher, T. L., Rodgers, K. B., Stock, C. A., & Cheung, W. W. L. (2016). Sources of uncertainties in 21st century projections of potential. *Ocean Ecosystem Stressors*, *30*(8), 1224–1243. https://doi.org/10.1002/2015gb005338

Garcia, H., Locarnini, R., Boyer, T., Antonov, J., Baranova, O., Zweng, M., & Johnson, D. (2010). Dissolved oxygen, apparent oxygen utilization, and oxygen saturation. *World Ocean Atlas 2009 NOAA Atlas Nesdis*, *70*, 28.

Garcia, H., Locarnini, R., Boyer, T., Antonov, J., Zweng, M., Baranova, O., et al. (2010). In S. Levitus (Ed.). *World ocean atlas 2009, volume 4: Nutrients (phosphate, nitrate, silicate), NOAA Atlas NESDIS 71*. U.S. Government Printing Office.

Giorgi, F., Coppola, E., Raffaele, F., Diro, G. T., Fuentes-Franco, R., Giuliani, G., et al. (2014). Changes in extremes and hydroclimatic regimes in the CREMA ensemble projections. *Climatic Change*, *125*(1), 39–51. https://doi.org/10.1007/s10584-014-1117-0

Giorgi, F., Jones, C., & Asrar, G. R. (2009). Addressing climate information needs at the regional level: The CORDEX framework. *World Meteorological Organization Bulletin*, *58*(3), 175.

Goebel, N. L., Edwards, C. A., Zehr, J. P., & Follows, M. J. (2010). An emergent community ecosystem model applied to the California. *Current System*, *83*(3–4), 221–241. https://doi.org/10.1016/j.jmarsys.2010.05.002

Gómez-Valdivia, F., Parés-Sierra, A., & Laura Flores-Morales, A. (2017). Semiannual variability of the California undercurrent along the southern California current system: A tropical generated phenomenon. *Journal of Geophysical Research: Oceans*, *122*(2), 1574–1589. https://doi.org/10.1002/2016jc012350

Griffies, S. M., Schmidt, M. A. R. T. I. N., & Herzfeld, M. I. K. E. (2009). Elements of mom4p1. GFDL ocean group Tech. *Rep*, *6*, 444.

Haidvogel, D. B., Arango, H., Budgell, W. P., Cornuelle, B. D., Curchitser, E., Di Lorenzo, E., et al. (2008). Ocean forecasting in terrain-following coordinates: Formulation and skill assessment of the regional Ocean modeling system. *Journal of Computational Physics*, *227*(7), 3595–3624. https://doi.org/10.1016/j.jcp.2007.06.016

Hall, A. (2014). Projecting regional change. *Science*, *346*(6216), 1461–1462. https://doi.org/10.1126/science.aaa0629

Hersbach, H., Bell, B., Berrisford, P., Hirahara, S., Horányi, A., Muñoz-Sabater, J., et al. (2020). The ERA5 global reanalysis. *Quarterly Journal of the Royal Meteorological Society*, *146*(730), 1999–2049. https://doi.org/10.1002/qj.3803

Hickey, B., MacFadyen, A., Cochlan, W., Kudela, R., Bruland, K., & Trick, C. (2006). Evolution of chemical, biological, and physical water properties in the northern California Current in 2005: Remote or local wind forcing? *Geophysical Research Letters*, *33*(22), L22S02. https://doi.org/10.1029/2006GL026782

Howard, E. M., Frenzel, H., Kessouri, F., Renault, L., Bianchi, D., McWilliams, J. C., & Deutsch, C. (2020). Attributing causes of future climate change in the California current system with multimodel downscaling. *Global Biogeochemical Cycles*, *34*(11). https://doi.org/10.1029/2020gb006646

Huyer, A., Barth, J. A., Kosro, P. M., Shearman, R. K., & Smith, R. L. (1998). Upper-ocean water mass characteristics of the California current, Summer 1993. *Deep Sea Research Part II: Topical Studies in Oceanography*, *45*(8), 1411–1442. https://doi.org/10.1016/S0967-0645(98)80002-7

Jacox, M. G., Bograd, S. J., Hazen, E. L., & Fiechter, J. (2015). Sensitivity of the California Current nutrient supply to wind, heat, and remote ocean forcing. *Geophysical Research Letters*, *42*(14), 5950–5957. https://doi.org/10.1002/2015gl065147

Kara, A. B., Rochford, P. A., & Hurlburt, H. E. (2000). An optimal definition for ocean mixed layer depth. *Journal of Geophysical Research*, *105*(C7), 16803–16821. https://doi.org/10.1029/2000jc900072

Kerkhoff, C., Künsch, H. R., & Schär, C. (2014). Assessment of bias assumptions for climate models. *Journal of Climate*, *27*(17), 6799–6818. https://doi.org/10.1175/jcli-d-13-00716.1

Kishi, M. J., Kashiwai, M., Ware, D. M., Megrey, B. A., Eslinger, D. L., Werner, F. E., et al. (2007). NEMURO—A lower trophic level model for the North Pacific marine ecosystem. *Ecological Modelling*, *202*(1–2), 12–25. https://doi.org/10.1016/j.ecolmodel.2006.08.021

Li, H., Kanamitsu, M., Hong, S.-Y., Yoshimura, K., Cayan, D. R., Misra, V., & Sun, L. (2014). Projected climate change scenario over California by a regional ocean–atmosphere coupled model system. *Climatic Change*, *122*(4), 609–619. https://doi.org/10.1007/s10584-013-1025-8

Liu, W. T. L., Katsaros, K., & Businger, J. (1979). 09/01 bulk parameterization of air-sea exchanges of heat and water vapor including the molecular constraints at the interface. *Journal of the Atmospheric Sciences*, *36*, 1722–1735. https://doi.org/10.1175/1520-0469(1979)036<1722:bpoase>2.0.co;2

Lynn, R. J., & Simpson, J. J. (1987). The California Current system: The seasonal variability of its physical characteristics. *Journal of Geophysical Research*, *92*(C12), 12947–12966. https://doi.org/10.1029/jc092ic12p12947

Machu, E., Goubanova, K., Le Vu, B., Gutknecht, E., & Garçon, V. (2015). Downscaling biogeochemistry in the Benguela eastern boundary current. *Ocean Modelling*, *90*, 57–71. https://doi.org/10.1016/j.ocemod.2015.01.003

Mote, P. W., & Mantua, N. J. (2002). Coastal upwelling in a warmer future. *Geophysical Research Letters*, *29*(23), 5351–5354. https://doi.org/10.1029/2002gl016086

Nam, S., Takeshita, Y., Frieder, C. A., Martz, T., & Ballard, J. (2015). Seasonal advection of Pacific Equatorial Water alters oxygen and pH in the. *Southern California Bight*, *120*(8), 5387–5399. https://doi.org/10.1002/2015jc010859

NASA Goddard Space Flight Center, Ocean Ecology Laboratory, Ocean Biology Processing Group. (2014). *SeaWiFS Ocean Color data; NASA Goddard space Flight center*. Ocean Ecology Laboratory, Ocean Biology Processing Group. https://doi.org/10.5067/ORBVIEW-2/SEAWIFS_OC.2014.0

Neveu, E., Moore, A. M., Edwards, C. A., Fiechter, J., Drake, P., Crawford, W. J., et al. (2016). An historical analysis of the California Current circulation using ROMS 4D-Var: System configuration and diagnostics. *Ocean Modelling*, *99*, 133–151. https://doi.org/10.1016/j.ocemod.2015.11.012

Oerder, V., Colas, F., Echevin, V., Codron, F., Tam, J., & Belmadani, A. (2015). Peru-Chile upwelling dynamics under climate change. *Journal of Geophysical Research: Oceans*, *120*(2), 1152–1172. https://doi.org/10.1002/2014JC010299

Pauly, D., & Christensen, V. (1995). Primary production required to sustain global fisheries. *Nature*, *374*(6519), 255–257. https://doi.org/10.1038/374255a0

Pierce, S. D., Smith, R. L., Kosro, P. M., Barth, J. A., & Wilson, C. D. (2000). Continuity of the poleward undercurrent along the eastern boundary of the mid-latitude north Pacific. *Deep Sea Research Part II: Topical Studies in Oceanography*, *47*(5), 811–829. https://doi.org/10.1016/S0967-0645(99)00128-9

Pozo Buil, M. (2023). Data from Evaluation of different bias correction methods for dynamical downscaled future projections of the California Current Upwelling System [Dataset]. Dryad. https://doi.org/10.5061/dryad.t1g1jwt8c

Pozo Buil, M., Jacox, M. G., Fiechter, J., Alexander, M. A., Bograd, S. J., Curchitser, E. N., et al. (2021). A dynamically downscaled ensemble of future projections for the California current system. *Frontiers in Marine Science*, *8*. https://doi.org/10.3389/fmars.2021.612874

Renault, L., Deutsch, C., McWilliams, J. C., Frenzel, H., Liang, J.-H., & Colas, F. (2016). Partial decoupling of primary productivity from upwelling in the California Current system. *Nature Geoscience*, *9*(7), 505–508. https://doi.org/10.1038/ngeo2722

Reynolds, R. W., Smith, T. M., Liu, C., Chelton, D. B., Casey, K. S., & Schlax, M. G. (2007). Daily high-resolution-blended analyses for sea surface temperature. *Journal of Climate*, *20*(22), 5473–5496. https://doi.org/10.1175/2007jcli1824.1

Ridgway, K. R., Dunn, J. R., & Wilkin, J. L. (2002). Ocean interpolation by four-dimensional weighted least squares—Application to the waters around Australasia. *Journal of Atmospheric and Oceanic Technology*, *19*(9), 1357–1375. https://doi.org/10.1175/1520-0426(2002)019<1357:oibfdw>2.0.co;2

Risien, C. M., Fewings, M. R., Fisher, J. L., Peterson, J. O., & Morgan, C. A. (2022). Spatially gridded cross-shelf hydrographic sections and monthly climatologies from shipboard survey data collected along the Newport Hydrographic Line, 1997–2021. *Data in Brief*, *41*, 107922. https://doi.org/10.1016/j.dib.2022.107922

Rudnick, D. L., Zaba, K. D., Todd, R. E., & Davis, R. E. (2017). A climatology of the California Current System from a network of underwater gliders. *Progress in Oceanography*, *154*, 64–106. https://doi.org/10.1016/j.pocean.2017.03.002

Rykaczewski, R. R., & Dunne, J. P. (2010). Enhanced nutrient supply to the California Current Ecosystem with global warming and increased stratification in an Earth system model. *Geophysical Research Letters*, *37*(21). https://doi.org/10.1029/2010gl045019

Rykaczewski, R. R., Dunne, J. P., Sydeman, W. J., García-Reyes, M., Black, B. A., & Bograd, S. J. (2015). Poleward displacement of coastal upwelling-favorable winds in the ocean's eastern boundary currents through the 21st century. *Geophysical Research Letters*, *42*(15), 6424–6431. https://doi.org/10.1002/2015gl064694

Shchepetkin, A. F., & McWilliams, J. C. (2005). The regional oceanic modeling system (ROMS): A split-explicit, free-surface, topography-following-coordinate oceanic model. *Ocean Modelling*, *9*(4), 347–404. https://doi.org/10.1016/j.ocemod.2004.08.002

Shin, S.-I., & Alexander, M. A. (2020). Dynamical downscaling of future hydrographic changes over the Northwest Atlantic ocean. *Journal of Climate*, *33*(7), 2871–2890. https://doi.org/10.1175/jcli-d-19-0483.1

Smith, J. A., Pozo Buil, M., Muhling, B., Tommasi, D., Brodie, S., Frawley, T. H., et al. (2023). Projecting climate change impacts from physics to fisheries: A view from three California current fisheries. *Progress in Oceanography*, *211*, 102973. https://doi.org/10.1016/j.pocean.2023.102973

Snyder, M. A., Sloan, L. C., Diffenbaugh, N. S., & Bell, J. L. (2003). Future climate change and upwelling in the California Current. *Geophysical Research Letters*, *30*(15). https://doi.org/10.1029/2003gl017647

Tapiador, F. J., Navarro, A., Moreno, R., Sánchez, J. L., & García-Ortega, E. (2020). Regional climate models: 30 years of dynamical downscaling. *Atmospheric Research*, *235*, 104785. https://doi.org/10.1016/j.atmosres.2019.104785

Taylor, K. E., Stouffer, R. J., & Meehl, G. A. (2012). An overview of CMIP5 and the experiment design. *Bulletin of the American Meteorological Society*, *93*(4), 485–498. https://doi.org/10.1175/bams-d-11-00094.1

Thomson, R. E., & Krassovski, M. V. (2010). Poleward reach of the California Undercurrent extension. *Journal of Geophysical Research*, *115*(C9). https://doi.org/10.1029/2010jc006280

Veneziani, M., Edwards, C. A., Doyle, J. D., & Foley, D. (2009). A central California coastal Ocean Modeling study: 1. Forward model and the influence of realistic versus climatological forcing. *Journal of Geophysical Research*, *114*(C4). https://doi.org/10.1029/2008jc004774

Wang, J., Swati, F. N. U., Stein, M. L., & Kotamarthi, V. R. (2015). Model performance in spatiotemporal patterns of precipitation: New methods for identifying value added by a regional climate model. *Journal of Geophysical Research: Atmospheres*, *120*(4), 1239–1259. https://doi.org/10.1002/2014jd022434

Xiu, P., Chai, F., Curchitser, E. N., & Castruccio, F. S. (2018). Future changes in coastal upwelling ecosystems with global warming: The case of the California Current System. *Scientific Reports*, *8*(1), 2866. https://doi.org/10.1038/s41598-018-21247-7

Xu, Z., Han, Y., & Yang, Z. (2019). Dynamical downscaling of regional climate: A review of methods and limitations. *Science China Earth Sciences*, *62*(2), 365–375. https://doi.org/10.1007/s11430-018-9261-5

Xu, Z., & Yang, Z.-L. (2012). An improved dynamical downscaling method with GCM bias corrections and its validation with 30 Years of climate simulations. *Journal of Climate*, *25*(18), 6271–6286. https://doi.org/10.1175/jcli-d-12-00005.1

Zaba, K. D., Franks, P. J. S., & Ohman, M. D. (2021). The California undercurrent as a source of upwelled waters in a coastal filament. *Journal of Geophysical Research: Oceans*, *126*(2). https://doi.org/10.1029/2020jc016602